Biophysical Journal
Article

Biophysical Society

Mapping Cell Membrane Fluctuations Reveals Their Active Regulation and Transient Heterogeneities

Arikta Biswas,[1] Amal Alex,[1] and Bidisha Sinha[1,*]
[1]Department of Biological Sciences, Indian Institute of Science Education and Research (IISER) Kolkata, Mohanpur, West Bengal, India

ABSTRACT Shape fluctuations of the plasma membrane occur in all cells, are incessant, and are proposed to affect membrane functioning. Although studies show how membrane fluctuations are affected by cellular activity in adherent cells, their spatial regulation and the corresponding change in membrane mechanics remain unclear. In this article, we study how ATP-driven activities and actomyosin cytoskeleton impact basal membrane fluctuations in adherent cells. Using interference imaging, we map height fluctuations within single cells and compare the temporal spectra with existing theoretical models to gain insights about the underlying membrane mechanics. We find that ATP-dependent activities enhance the nanoscale z fluctuations but stretch out the membrane laterally. Although actin polymerization or myosin-II activity individually enhances fluctuations, the cortex in unperturbed cells stretches out the membrane and dampens fluctuations. Fitting with models suggest this dampening to be due to confinement by the cortex. However, reduced fluctuations on mitosis or on ATP-depletion/stabilization of cortex correlate with increased tension. Both maps of fluctuations and local temporal autocorrelation functions reveal ATP-dependent transient short-range (<2 μm) heterogeneities. Together, our results show how various ATP-driven processes differently affect membrane mechanics and hence fluctuations, while creating distinct local environments whose functional role needs future investigation.

INTRODUCTION

Plasma membrane deformations are associated with several of its functions such as motility, cell division, vesicle trafficking, mechanoresponse, etc. (1,2). Fluctuation spectra of deformations capture parameters responsible for deformability of the membrane. Governed by viscoelastic properties of the membrane, fluctuations are powered by thermal energy as well as ATP-driven processes. The temporal range of fluctuations reported is quite broad. Slow (10 s) actin waves drive large wavelength fluctuations (100 nm–10 μm) at cell edges and basal membrane (3–5). They are accompanied by fluctuations with relatively smaller amplitudes (5–50 nm) that are more prominently observed at basal membrane (6–8), and are mainly thermal in nature. Although larger amplitudes are involved in cell spreading and motility (3,4,9), studies suggest that thermal fluctuations (<10 nm) can influence the spatial organization of molecules on membranes leading to formation of nanodomains/invaginations (10,11).

In contrast to cell edges, fluctuations of the rest of the basal membrane of nucleated adherent cells remain lesser explored (6–8,12,13). However, its amenability to a variety of imaging techniques makes the basal membrane an ideal platform to study the properties and functional implications of shorter fluctuations. Dynamics of the basal membrane can be studied in terms of its height (distance from substrate in z direction) fluctuations (14). Studies demonstrate amplitudes to be 10s of nanometers and fluctuations to be affected by ATP depletion and cytoskeleton perturbation (6–8,12,13). However, these studies have either explored the power spectral density of fluctuations in monolayers with no spatial resolution (12,13) or have focused on only the temporal (7) or spatial (8) aspects in single cells—rarely combining the two for broad range of timescales (5,6). The power of combining them has already been demonstrated in red blood cells (RBCs) for differentiating nonthermal from thermal fluctuations (15,16). To be able to understand the spatial regulation of lipid/protein organization by fluctuations, their spatial heterogeneities cannot be ignored in experiments.

At the basal membrane of nucleated adherent cells, ATP-dependent processes have been shown to increase the

Submitted February 16, 2017, and accepted for publication August 21, 2017.

*Correspondence: bidisha.sinha@iiserkol.ac.in

Amal Alex's present address is Department of Mechanistic Cell Biology, Max Planck Institute of Molecular Physiology, Dortmund, North Rhine-Westphalia, Germany.

Editor: Cecile Sykes.

http://dx.doi.org/10.1016/j.bpj.2017.08.041

amplitude of fluctuations while making distributions non-Gaussian (7). However, how ATP-dependent processes alter the landscape and heterogeneity of fluctuations is yet to be established. The effect of the actomyosin network on spatio-temporal regulation of fluctuations also remains unclear with both reports of increase (6) and decrease of fluctuations (12). Unlike the spectrin network of RBCs, actin-based structures across a single nucleated adherent cell form heterogeneous patterns that modulate the height profile (undulations) of the membrane (17). How does the cortex and its activities—actin polymerization, myosin-II motor activity—affect the landscape of fluctuations and their heterogeneities? To address this, the impact of cortex on spatial distribution of fluctuations along with measurements of corresponding alteration in membrane mechanics need to be studied.

We address these issues by working with HeLa, CHO (epithelial), and C2C12 (myoblast) cells. Adapting a noninvasive imaging technique, interference reflection microscopy (IRM) (18–22), we measure spatio-temporal parameters of membrane z fluctuations at high z- but diffraction-limited xy-resolution. The impacts of ATP-driven processes and cortex on fluctuations are probed by drug-based perturbations and the temporal spectra are compared with existing theoretical models.

MATERIALS AND METHODS

Cell culture and fixation

HeLa, CHO-K1, and C2C12 cells are grown in Dulbecco's Modified Essential Medium (Gibco/Life Technologies, Carlsbad, CA) supplemented with 10% fetal bovine serum (Gibco/Life Technologies) and 0.4% Pen/Strep L-Glutamine mixture (Lonza, Basel, Switzerland) and maintained at 37°C in a humidified atmosphere with 5% CO_2. Cells, used between passages 3 and 17, are deposited on customized glass-bottomed dishes at a concentration of ~20,000 cells/mL and all experiments are performed after 12–16 h of seeding. For actin labeling, cells are fixed with 4% paraformaldehyde (Sigma-Aldrich, St. Louis, MO) for 15 min, washed thoroughly with 1× phosphate-buffered saline (Sigma-Aldrich), and then incubated in 0.1 M glycine (Sigma-Aldrich) for 5 min. They are washed well and then incubated with 1 μM AlexaFluor 488 Phalloidin (Molecular Probes; Invitrogen, Carlsbad, CA) in the dark for 45 min. To visualize the nucleus in live cells, cells are incubated with 1 μg/mL Bisbenzimide Hoechst 33342 (Sigma-Aldrich) at 37°C for 30 min (23). Cells are always washed before imaging.

Pharmacological treatments

Specific agents are used to inhibit the polymerization of actin filaments, i.e., cytochalasin D and latrunculin B (Cyto D and Lat B; Sigma-Aldrich) and blebbistatin (Blebb.) to inhibit myosin-II activity (Sigma-Aldrich). Quantities of 2-deoxy D-glucose and sodium azide (Sigma-Aldrich) are used to deplete ATP, and Jasplakinolide (Jas; Molecular Probes) is used to stabilize preexisting actin filaments by favoring polymerization. Cells are grown and treated separately for 1 h with 5 μM Cyto D (24), 5 μM Lat B (25), 100 μM blebbistatin (26), and 5 μM Jas (27). Quantities of 10 mM sodium azide and 10 mM 2-deoxy D-glucose are added to cells (28) in M1 Imaging medium (150 mM NaCl; Sigma-Aldrich), 1 mM $MgCl_2$ (Merck, Kenilworth, NJ), and 20 mM HEPES (Sigma-Aldrich) and incubated for 60 min for ATP depletion (dep.). All the incubations are done at 37°C.

Transfection

pEGFP-MRLC1 is a gift from Tom Egelhoff (Addgene plasmid: 35680) (29). A quantity of 1 μg of the plasmid DNA is transfected into the HeLa cells to label the myosin-II in live cells by Lipofectamine 3000 (Life Technologies) as per manufacturer protocol. Cells are imaged 16 h posttransfection.

Formation of plasma membrane spheres

Cells are grown on micropatterns (clusters of 64 hexagons each with a side of 18 μm separated by 40 μm). For micropatterning, etched coverslips are first coated with PLL-g-PEG (SuSoS, Dübendorf, Switzerland) and then selectively depleted of PLL-g-PEG by UVO treatment (UVO Cleaner; Jelight, Irvine, CA) at the desired locations using Photomask (JD Photo Data, Hitchin, United Kingdom), as in (30). The coverslips are washed thoroughly and used for cell culture. Cells at ~70% confluency are incubated for 6–8 h in phosphate-buffered saline (at pH 7.4) supplemented with 1.5 mM $CaCl_2$ (Sigma-Aldrich), 1.5 mM $MgCl_2$ (Merck), and 10 mM MG132 (Sigma-Aldrich) at 37°C (31). The sample is directly imaged for measuring fluctuations on cell-attached and cell-free plasma membrane spheres (PMSs).

Imaging techniques

An Eclipse Ti-E motorized inverted microscope (Nikon, Tokyo, Japan) equipped with adjustable field and aperture diaphragms, 60× Plan Apo (NA 1.22, water immersion), a 1.5× external magnification, and an electron-multiplying charge-coupled device camera (Evolve 512 Delta; Photometrics, Trenton, NJ) is used for imaging in differential interference contrast, epifluorescence, and IRM modes. For IRM, an additional 100 W mercury arc lamp, an interference filter (546 ± 12 nm), and a 50:50 beam splitter is used. Cells and beads (60 μm in diameter; Bangs Laboratories, Fishers, IN) are imaged in 3 mL Dulbecco's Modified Essential Medium, No-Phenol Red in a 37°C onstage incubator at EM gain 30 and exposure time 50 ms. All movies are recorded at the same settings for 102 s at 19.91 frames/s (2048 frames).

Total internal reflection fluorescence (TIRF) images are acquired using a CMOS camera (ORCA-Flash4.0; Hamamatsu, Hamamatsu City, Japan) attached to a TIRF microscope, based on an IX-83 inverted microscope (Olympus, Melville, NY) equipped with a 100× NA 1.49 oil-immersion objective (PlanApo; Olympus) and a 488-nm laser. All images are acquired at exposure time 300 ms and penetration depth of 100 nm.

Calculation of spatio-temporal parameters

The software MATLAB (The MathWorks, Natick, MA) is used to calculate the relative height at all time-points for each pixel from the $\Delta I/\Delta h$ conversion factor (Supporting Discussion) of the day's alignment. The SD from the relative heights across 144 pixels (2.16×2.16 μm^2) in a first branch region (FBR) is calculated, averaged over 20 frames, and termed as $SD_{(space)}$. For each pixel, the relative height time-series is obtained. The mean and SD of the time-series are calculated, averaged across 144 pixels in an FBR, and termed as mean relative height and $SD_{(time)}$. The power spectral density (PSD) of the height time-series for each pixel is subsequently calculated from a custom-written program using the FFT algorithm provided by MATLAB and averaged across an FBR. The area under the curve of PSD is calculated each time and matched with the variance of the time-series as a check. The root of the area under the PSD curve of frequency bands of 0.01–0.1 Hz and 0.1–1 Hz are calculated and

termed as $\overline{\sigma}$. The log (PSD) versus log(f) is fitted to a straight line for frequencies from 0.04 to 0.4 Hz. The slope of the fit is termed as the exponent. PSD_{cell} is calculated by averaging PSD curves of all FBRs in a cell. A 60 × 60 pixels noncell region is chosen to calculate $PSD_{background}$. The ratio of the background-subtracted PSD of treated cells to control cells $f = (PSD_{cell(treated)} - PSD_{background(treated)}/PSD_{cell(untreated)} - PSD_{background(untreated)})$ is plotted as a function of frequency. Spatial autocorrelation functions (ACF) are calculated as $G(r) = \langle \Delta h(r')\Delta h(r'+r)\rangle / \langle \Delta h(r')^2 \rangle$ in long FBRs (35 × 10 pixels corresponding to 6.3 × 1.8 μm^2) and averaged in 200 frames. Temporal ACFs are calculated over 2048 frames as $G(t) = \langle \Delta h(t')\Delta h(t'+t)\rangle / \langle \Delta h(t')^2 \rangle$ and averaged across small FBRs of 2 × 2 pixels (0.36 × 0.36 μm^2). Spatial and temporal ACFs are fitted with a three-term multiexponential function to obtain the correlation length (λ) and time (τ), respectively; PSDs are fitted with a modified theoretical model to extract mechanical parameters. Gaussian-ness of temporal fluctuations is evaluated at each pixel by Kolmogorov-Smirnov hypothesis testing (Supporting Discussion).

Analysis of heterogeneity in cells

The $SD_{(time)}$ for each pixel is collated across 144 pixels in an FBR, and the SD of the series is averaged over multiple FBRs in a cell and termed as $SD(SD_{(time)})$. It is used as a measure of short length-scale heterogeneity inside an FBR. The $SD_{(time)}$ of all 144 pixels in an FBR is compared to those of other FBRs in pairs, and a one-way analysis of variance (ANOVA) is performed. If p value is <0.001, $SD_{(time)}$ maps are dissimilar. The number of such FBR pairs with dissimilar $SD_{(time)}$ is counted and the ratio of such pairs to the total number of FBR pairs in a cell is calculated and termed as percent dissimilarity. This parameter is used as a measure of long length-scale heterogeneity.

Analysis of the amount of cortex present in cells

The periphery of an actin-stained epi-fluorescent cell is marked in the software ImageJ (National Institutes of Health, Bethesda, MD), linearized, and the total length is measured. The cortical regions in the cell having a signal-to-noise ratio >2 are marked, the lengths of each is added, and it is considered as cortex. The ratio of the amount of cortex present to the total periphery is calculated and averaged over 10 cells.

Statistical analysis

Calibration with beads and control experiment with cells without any treatment is performed with each set of experiment. During time-lapse imaging for any set, at least 10 cells are imaged for each condition and ~20–40 FBRs analyzed for each cell. In most cases, analysis is collated over at least three sets of experiments performed on different days. For comparisons between populations of cells, a one-way ANOVA combined with a Tukey post-hoc test is performed to determine the statistical significance (*p < 0.05, ** p < 0.001) whenever the parameters have similar variances and have Gaussian distributions. A Mann-Whitney U test is done whenever the parameters are not Gaussian.

RESULTS

Using interference microscopy to map membrane dynamics

To quantify basal membrane fluctuations, adherent eukaryotic cells are imaged using IRM (Fig. 1 *a*). The interference pattern in an IRM image of a cell is produced by light reflected off from the coverslip and the reflected beam from the plasma membrane (due to the differences in the refractive indices). Thus, the intensity of the interference image, at any pixel and time, can be used to measure the height of the membrane patch at that pixel and time. For calculating spatio-temporal height variations, first, the intensity variation (ΔI) to height variation (Δh) is obtained by calibrating with an object whose height profile is known. Second, parts of the cell where this conversion is applicable are identified and corresponding maps of relative height ($\Delta h + h_0$) are obtained.

For the calibration of ΔI to Δh conversion, a 60 μm polystyrene bead is imaged (Fig. 1 *b*, *top*; and Supporting Discussion). Its interference pattern displays Newtonian rings (Fig.1 *b*, *top*) due to the radial symmetry in its monotonically increasing height profile from the center. The intensity dependence on height shows periodicity (Fig.1 *b*, *bottom*) as expected (22)—leading to degeneracy in height prediction from intensity because a particular intensity is repeated at different branches and hence at different heights. We restrict our analysis to regions that lie within the first branch of the profile (Fig. 1 *b*) to make the conversion possible. The central part of the first branch can be approximated to have linear intensity height dependence as depicted in the linear fit (Fig. 1 *b*, *bottom*). For a given wavelength and refractive index of external medium, the slope is expected to depend on the difference (D) of intensity of maxima (I_{max}) and minima (I_{min}) of the first branch (Fig. 1 *b*, *bottom*; Supporting Discussion). Beads are imaged at various exposure times to cover a range of I_{max} and I_{min}—hence, D and S (= I_{max} + I_{min}; Fig. 1 *c*, *top*). The corresponding slopes show a linear dependence on exposure time (Fig. 1 *c*, *bottom*) that allows calculation of slopes for intermediate values of exposure times. Next, IRM images of HeLa cells (Fig. 1 *d*) are analyzed to obtain I_{max} and S/2. The S/2 value (cross-checked in three different ways, Fig. S1 *a–c*; Supporting Discussion) is compared with those obtained from beads and the corresponding slope read out. The corresponding D for the cell (= $2I_{max} - S$) matches closely with that of the bead and hence justifies the conversion (Fig. 1 *e*; Table S1). Typically, the conversion entails ~20,400 ± 9900 intensity units for 100 nm (~204 units/nm). The resolution is thus ~6 nm for relative height measurement as the noise is 1200 intensity units. However, our analysis relies on height fluctuations captured by $SD_{(time)}$. $SD_{(time)}$ is measured to be ~2 nm for background regions and ~0.5 nm for dark current (imaging without light source)—this sets the minimum resolvable $SD_{(time)}$. But, variations (~2 nm) observed in $SD_{(time)}$ measured over different days have no correlation with the ΔI to Δh conversion used (Fig. 1 *f*), and hence reflect the inherent variability in HeLa cells.

Next, FBRs in the cell are identified (Supporting Discussion) by accepting groups of pixels that meet the two following criteria. The first is to only allow a range of intensities (I_{min} + 2000 to I_{max} − 2000) so that pixels

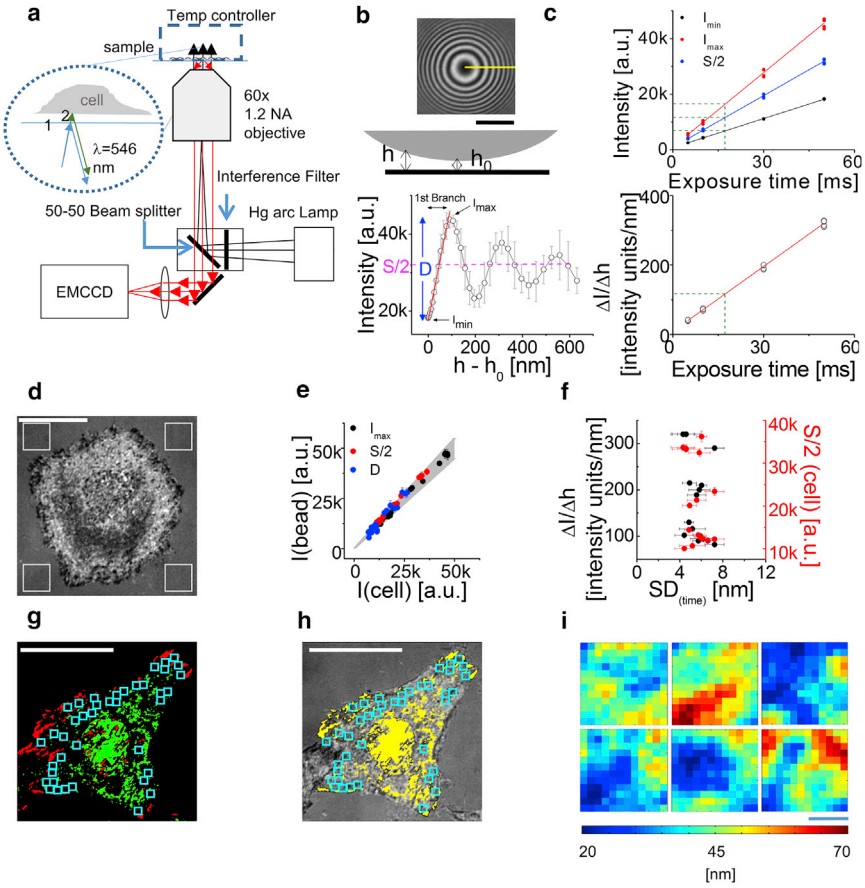

FIGURE 1 Details of calibration of IRM. (*a*) Given here is an IRM setup schematic showing illumination and detection path. Zoomed-in view shows reflections at interface 1 (coverslip-medium, *blue arrows*) and 2 (medium-cell, *green arrows*), which interfere. (*b*) (*Top*) Shown here is an IRM image of a bead with a typical radial line in yellow. (*Bottom*) Shown here is an averaged intensity-versus-height profile ($N = 10$) with linear fit of the first branch in red. (*c*) (*Top*) Shown here is a plot of I_{max}, I_{min} and S/2 from profiles of same beads is imaged at different exposure times ($n = 5$ beads, four line scans per bead) for a particular day. (*Bottom*) Given here is $\Delta I/\Delta h$ versus exposure times for beads. (*d*) Shown here is a typical IRM image of a HeLa cell. White ROIs are used to calculate S/2 (cell). (*e*) Given here is a comparison of I_{max}, I_{min} and S/2 between beads and cells for different days ($N = 20$). Gray region covers $y = x \pm 0.1\,x$. (*f*) Shown here is the $SD_{(time)}$ measured and the S/2 (cell) used for different days versus the conversion ($\Delta I/\Delta h$) used. (*g*) Shown here are minima (*red*) and maxima (*green*) projections of an HeLa cell with FBRs overlaid in cyan. (*h*) Shown here, FBRs are overlaid on the corresponding IRM image. (*i*) Shown here are relative height maps at any given time-point of six FBRs in an HeLa cell. Scale bars represent 1 μm. Scale bars for (*a–h*) = 10 μm. See also Fig. S1; Supporting Discussion. To see this figure in color, go online.

corresponding to interference maxima and minima are excluded. However, this is not enough to filter out pixels whose heights correspond to higher-order branches. The second criterion enforced is to choose regions of interest (ROIs) any of whose edges could be physically connected (1-pixel distance) to the first minima. The projection of first minima (*red pixels*, Fig. 1 *g*) and first maxima (*green pixels*, Fig. 1 *g*) from time-lapse images are used as a guide to the eye for selecting FBRs (pixels in the cell not marked in *yellow*; Fig. 1 *h*). We find that an $\sim$73 $\pm$ 10% ($N = 30$ cells) area of the cell is FBRs. However, for consistency in analysis, we use multiple square FBRs (12 $\times$ 12 pixels) per cell that amount to $\sim$10 $\pm$ 4% ($N = 30$ cells) of the basal membrane (*cyan ROIs*; Fig. 1, *h* and *i*).

IRM images, without conversion, themselves reveal interesting features that qualitatively describe the membrane topology. Whereas images of RBCs show circular symmetry, adherent eukaryotic cells show a different and heterogeneous topology (Fig. S2). Focal adhesions appear commonly as dark patches and the membrane under the nucleus appears at a higher contrast—often displaying mobile particulate features (Movies S1 and S2).

Time-lapse imaging of cells reveals intensity flickering at all pixels (Fig. S3). Relative heights (Fig. 2 *a*(*i*)) obtained from intensities are compared either across space (Fig. 2 *a*(*ii* and *iii*)) or time (Fig. 2 *a*(*iv–viii*)) to calculate the different parameters, ACFs and PSDs. The amplitudes of spatial undulations and temporal fluctuations are quantified by $SD_{(space)}$ and $SD_{(time)}$, respectively. Because the PSD captures the distribution of fluctuations over various frequencies, $\overline{\sigma}$ values for frequency ranges 0.01–0.1 Hz and 0.1–1 Hz are calculated to compare fluctuation levels at lower and higher frequencies. The exponent, also computed from the PSD, reveals the power-law dependence of PSD on frequency in the 0.04–0.4 Hz band. The values λ and τ are calculated by fitting spatial and temporal ACFs to three-term multiexponentials, respectively. Mechanical parameters are extracted by fitting PSDs to theoretical models (Fig. 2 *a*(*viii*)). Finally, $SD_{(time)}$ of whole cells (non-FBR regions blocked out) as well as square FBRs (used for computing the parameters; Fig. 2 *b*) are mapped to quantify the spatial profile of the temporal fluctuations.

In HeLa cells, we find $SD_{(time)}$ to be $\sim$4.9 $\pm$ 0.7 nm and $SD_{(space)}$ to be $\sim$7.2 $\pm$ 1.5 nm (Figs. 2 and S4). $SD_{(time)}$ and PSD (Fig. S3 *b* and *c*) remain similar over different days as well as different batches with minor variations. Similar values for spatio-temporal parameters are seen in two other cell types—CHO and C2C12 (Fig. S4). In comparison,

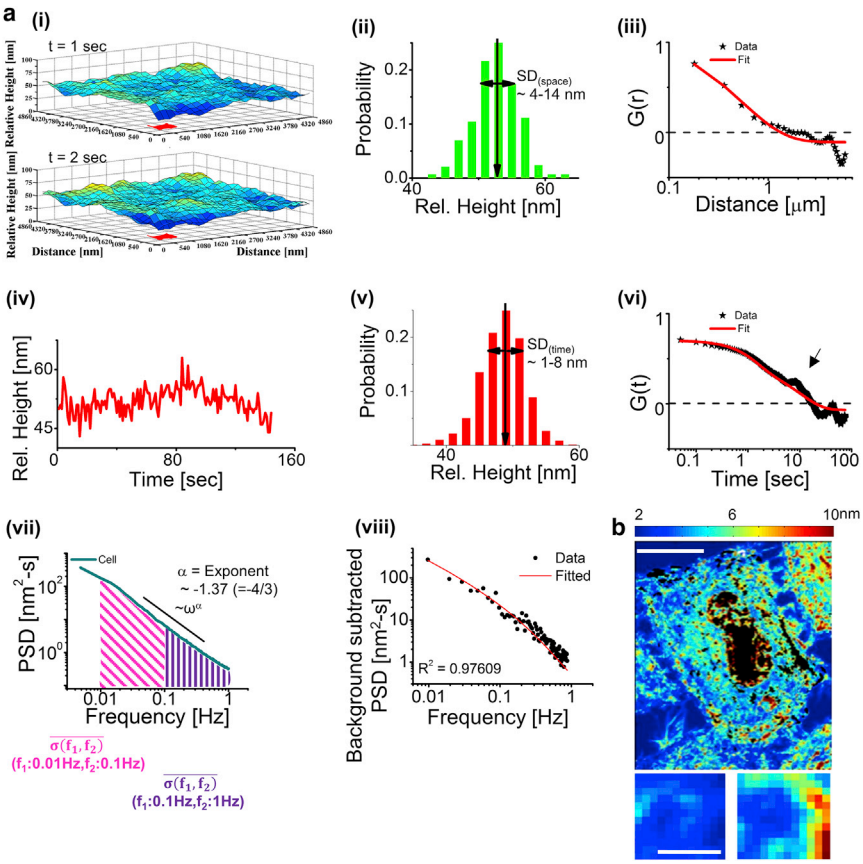

FIGURE 2 Quantification of temporal fluctuations and spatial undulations. (*a*) (*i*) Given here is a relative height map of a membrane patch (FBR) at two time-points. (*ii*) Shown here is a distribution of relative heights across the FBR at any particular time-point. (*iii*) Representative spatial ACF is measured at a long FBR. Solid line shows fit to three-term multiexponential function. (*iv*) Given here is a time-series of relative heights of a pixel in red in (*i*). (*v*) Distribution of relative heights is given for a time-series in (*iv*). (*vi*) Shown here is a representative temporal ACF of a small FBR. Solid line shows fit to a three-term multiexponential function. Black arrow points out a bump. (*vii*) Given here is a PSD at an FBR, and the parameters extracted from it. (*viii*) Fitting of a background-subtracted PSD was made to Eq. 1. (*b*) Shown here are $SD_{(time)}$ maps of an HeLa cell (non-FBRs blocked by white; scale bars, 10 μm) and two FBRs. Scale bars, 1 μm. To see this figure in color, go online.

amplitudes of temporal fluctuations reported in RBCs (32) are ~20–30 nm and amplitudes of spatial undulations reported in MDA-MB-231 epithelial cells are ~8–11 nm (8). The observed λ of ~500 nm (Fig. 2 *a*; Table S2) is lower than predicted values (~600 nm) (33). We find a $f^{-4/3}$ dependence of the PSD for frequency range 0.04–0.4 Hz (Fig. 2 *a*; Table S2), which is associated in the literature with hydrodynamic damping by a rigid wall (34,35). The correlation between $SD_{(time)}$ and mean relative height from the substrate (Fig. S3, *d–f*) is found to be weak, suggesting that damping by the rigid substrate is not the dominant factor controlling fluctuations.

We next investigated the role of ATP-dependent processes in regulating fluctuations.

ATP-driven activities increase temporal fluctuations and flatten out spatial undulations

Membrane fluctuations are expected to be due to thermal as well as ATP-dependent processes (32,36,37). Work on fluctuations in the cytoplasm have already shown that ATP-dependent processes generate random noise (38–40). To ascertain the contribution of ATP-driven processes, cells are depleted of ATP. To strengthen this, effects of Staurosporine induced cell death and fixation is tested. Although ATP depletion and cell death block the main source of active energy in cells, fixation stops all biochemical activities and additionally rigidifies the cell without triggering biochemical responses (Figs. 3 *a* and S5 *a*). In all three cell lines, the three treatments show a net reduction in temporal fluctuations (Figs. 3, *b* and *c*; S5 *b*, S6, and S7; Movie S3). The complete frequency dependence of weakened temporal fluctuations is plotted as f (ratio of the background-subtracted PSD of treated set to control) in which $f = 1$ represents no change whereas $f > 1$ and $f < 1$ represent increased and decreased fluctuations from control cells, respectively. On ATP depletion, Staurosporine treatment, or fixation, f is reduced over a broad range of frequencies (Fig. 3 *b*, *insets*). The exponent is close to -1 and reflects increased damping on all treatments (Figs. S5 *b*, S6, and S7). In contrast to $SD_{(time)}$, $SD_{(space)}$ is seen to increase in all the treatments (Figs. 3 *d*, S6, and S7). The average λ of ATP-depleted cells shows a significant reduction (Fig. 3 *e*) and the distribution of τ shows underrepresentation of timescales ranging from 0.2–2 s (Fig. 3 *f*). The normality of fluctuations (evaluated for each pixel, expressed as p value) shows that ATP depletion increases the Gaussian-ness of fluctuations (Fig. 3 *g*). Thus, cellular activity enhances the temporal fluctuations, altering their nature while decreasing the spatial amplitudes and flattening the membrane.

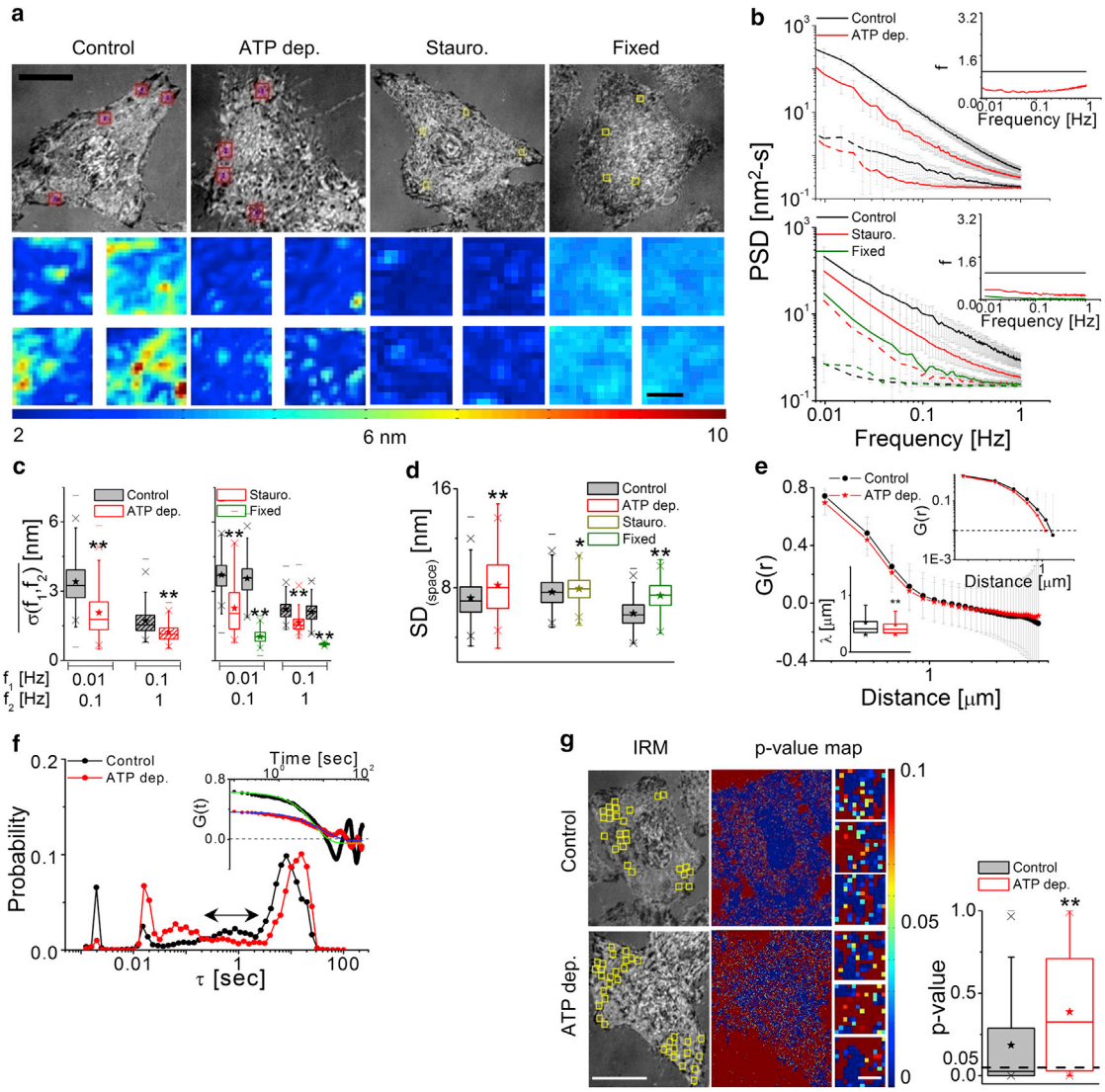

FIGURE 3 Effect of prevention of cellular activity on membrane fluctuations. (*a*) Shown here are IRM images (scale bars, 10 μm) and $SD_{(time)}$ maps (scale bars, 1 μm) of FBRs in control, ATP-depleted, staurosporine-treated (Stauro., 5 μM, 60 min), and fixed HeLa cells. (*b*) Given here are PSDs of FBRs in treated cells and their controls (*solid lines*) with their backgrounds (*dashed lines*); inset shows the value *f*. (*Top*) Shown here are $N = 50$ cells each, $n_{control} = 1083$ FBRs, and $n_{ATP\ depletion} = 880$ FBRs. (*Bottom*) Shown here are $N = 10$ cells each, $n_{control} = 412$ FBRs, $n_{staurosporine} = 336$ FBRs, and $n_{fixed} = 329$ FBRs. (*c* and *d*) Given here are temporal and spatial parameters for (*b*). $^{*}p < 0.05$, $^{**}p < 0.001$, one-way ANOVA. (*e*) Shown here are averaged spatial ACFs (and their log-log plots, *top inset*) for control and ATP-depleted cells ($N = 80$ cells, $n_{control} = 2024$ FBRs, and $n_{ATP\ depletion} = 1244$ FBRs). (*Bottom inset*) Given here are correlation lengths. (*f*) Weighted distribution of correlation timescales was obtained from temporal ACFs (*inset*: *solid line* shows fits) ($N = 9$ cells, $n_{control} = 3765$ FBRs, and $n_{ATP\ depletion} = 1987$ FBRs). (*g*) Given here are IRM images (scale bars, 20 μm), with FBRs overlaid in yellow and their corresponding *p*-value maps (Kolmogorov-Smirnov hypothesis testing). Scale bars, 1 μm. (*Right*) Given here is the *p* value for FBRs in control versus ATP-depleted cells. Shown here are $N = 30$ cells, $n_{control} = 41{,}760$ pixels, and $n_{ATP\ depletion} = 25{,}766$ pixels. Asterisks in (*e*) and (*g*) indicate $^{**}p < 0.001$, Mann-Whitney U test. See also Figs. S5 and S7; Tables S2 and S3. To see this figure in color, go online.

The actomyosin cortex has dynamic connections with the membrane (41,42), is home to various ATP-driven processes, and is the next target of our study.

Active cortex stretches out membrane but has dual effect on temporal fluctuations

Actin polymerization (can extend the membrane by ~2.76 nm per polymerization depending on the angle of polymerization (43)) and the organization of short actin filaments by myosin-II (44) can enhance membrane fluctuations. In contrast, pinning of the membrane onto a much tensed actomyosin cortex and presence of contractile stress fibers can reduce deformability and have an opposite effect. How the cortex affects membrane fluctuations therefore depends on the locally dominant process.

We block actin polymerization by Cyto D or Lat B, and block actin dynamics by Jas. We find that the PSDs and

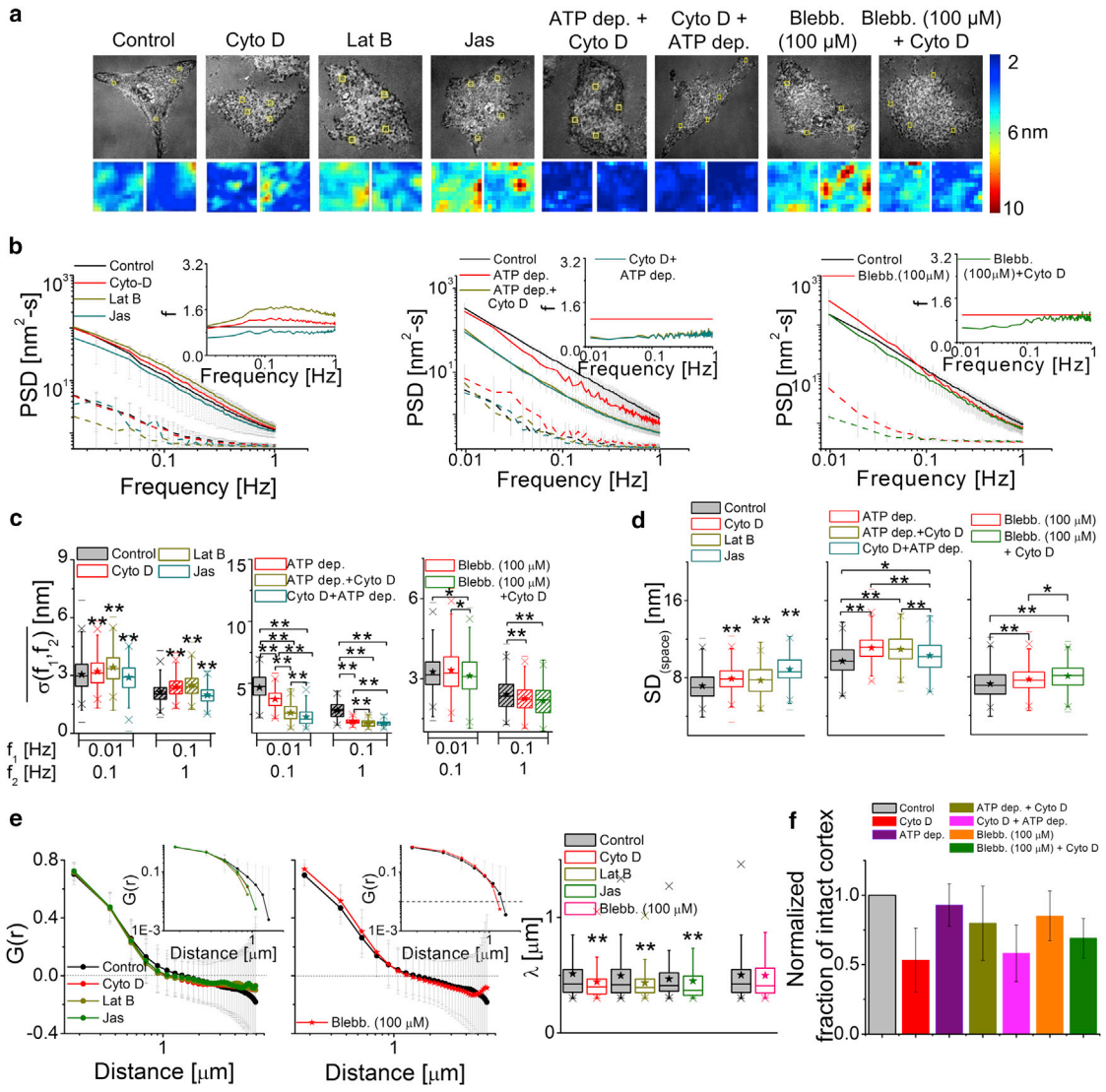

FIGURE 4 Effect of the actomyosin cortex on membrane fluctuations. (*a*) Given here are IRM images (scale bars, 10 μm) and $SD_{(time)}$ maps (scale bars, 1 μm) of HeLa cells under mentioned conditions. (*b*) Shown here are PSDs for cells (*solid lines*) and their backgrounds (*dashed lines*), with the inset showing the value *f* for all conditions. (*Left*) Shown here are $N = 30$ cells each, $n_{control} = 741$ FBRs, $n_{Cyto\ D} = 564$ FBRs, $n_{Lat\ B} = 426$ FBRs, and $n_{Jas} = 259$ FBRs. (*Middle*) Shown here are $N = 10$ cells each, $n_{control} = 141$ FBRs, $n_{ATP\ depletion} = 158$ FBRs, $n_{ATP\ depletion\ +\ Cyto\ D} = 254$ FBRs, and $n_{Cyto\ D\ +\ ATP\ depletion} = 162$ FBRs. (*Right*) Shown here are $N = 20$ cells each, $n_{control} = 402$ FBRs, $n_{blebbistatin} = 333$ FBRs, and $n_{blebbistatin\ +\ Cyto\ D} = 193$ FBRs. (*c* and *d*) The parameters of temporal fluctuations and spatial undulations of cells are given under different conditions. $*p < 0.05$, $**p < 0.001$, one-way ANOVA. (*e*) Given here are averaged spatial ACFs (and their log-log plots, *top inset*) and correlations lengths ($n_{control} = 1085$ FBRs, $n_{Cyto\ D} = 494$ FBRs, $N = 40$ cells each; $n_{control} = 884$ FBRs, $n_{Lat\ B} = 495$ FBRs, $N = 30$ cells; $n_{control} = 300$ FBRs, $n_{Jas} = 102$ FBRs, $N = 20$ cells; and $n_{control} = 811$ FBRs, $n_{blebbistatin} = 729$ FBRs, $N = 30$ cells). $*p < 0.05$, $**p < 0.001$, Mann-Whitney U test. (*f*) Given here is the normalized fraction of cortex clearance ($N = 10$ cells each). See also Figs. S8, S9, S10, S11, and S12; Tables S2 and S3. To see this figure in color, go online.

$SD_{(time)}$ show a net enhancement of temporal fluctuations for Cyto D and Lat B but reduction for Jas (Figs. 4, *a–c*, and S8; Movie S3). Both *f* (Fig. 4 *b*, *inset*) and $\overline{\sigma}$ (Fig. 4 *c*) reflect that both lower and higher frequencies are affected, although the effect is not as uniform over the frequencies as in ATP depletion. However, larger amplitudes of spatial undulations (Fig. 4 *d*) and shorter λ-values (Fig. 4 *e*) are observed in all these treatments. Quantifications show that there is an $\sim$47 $\pm$ 22% loss of defined cortex from the vicinity of the membrane after Cyto D treatment (Figs. 4 *f* and S9). Thus, absence of an intact cortex enhances, but blocking actin dynamics reduces, fluctuations. To understand why reducing polymerization rates by Cyto D also does not reduce fluctuations, we study the effect of polymerization without affecting cortex integrity.

We recreate a condition in which the cortex remains intact but polymerization is blocked. Cortex clearance on Cyto D treatment requires forces generated by actomyosin contractility (45). Blocking myosin-II activity by ATP

depletion or blebbistatin (100 μM) treatment before addition of Cyto D shows that only 20 $\pm$ 27% and 21 $\pm$ 14% of the cortex is cleared, respectively (Figs. 4 *f* and S9). The subsequent effect of Cyto D on these pretreated cells is reversed. Temporal fluctuations are now reduced instead of being amplified (Figs. 4, *a–c*, S10, and S12). On reversing the order of treatments (Cyto D + ATP depletion) cortex clearance (42 $\pm$ 20%) is observed along with reduction in fluctuations (Figs. 4, *a–c* and S10). Thus, polymerization individually can enhance fluctuations. The role of myosin-II motor activity at the cortex is investigated next.

Blocking myosin-II motors shows that blebbistatin at low concentration (5 μM, 60 min) either does not change or it decreases the temporal fluctuations (Fig. S11; Movie S3). The global actin distribution (Fig. S9 *a*) is not affected at this concentration, implying that local myosin-II activities have a positive contribution to fluctuations. At 100 μM, fluctuations either do not change or are significantly enhanced (Figs. 4, *a–c* and S12; Movie S3). The global actomyosin distribution at this concentration appears more diffused (Fig. S12 *a*). Hence, the positive contribution of myosin-II activity on fluctuations are measurable when the cortex is not globally altered by blebbistatin.

In all the above treatments, although the $SD_{(time)}$ either increases or decreases, the $SD_{(space)}$ always increases (Fig. 4 *d*). Additionally, λ (Fig. 4 *e*) decreased for Cyto D, Lat B, and Jas (although not for blebbistatin (100 μM)). Decreased $SD_{(space)}$ and increased λ in unperturbed cells imply that the cytoskeleton flattens membrane undulations.

We thus show that, in interphase cells, although polymerization- or myosin-II-based activities can enhance temporal fluctuations, the net contribution of the cortex is to dampen fluctuations that are dependent on cortex integrity and contractility (Tables S2, S3, and S4). We next explore systems where the membrane is at a different mechanical state than interphase cells and the cortex is either stiffer or completely missing.

Reduced spatio-temporal fluctuations in mitotic cells and PMSs

Mitotic cells, their cortex (Fig. 5, *a* and *b*), and PMSs (Fig. 5 *c*) are imaged to study membrane fluctuations. Mitotic cells have increased apparent membrane tension compared to interphase cells (46), which are known to not alter on cytoskeleton perturbation—thus indicating a higher level of bilayer tension than interphase cells. These cells have a more cross-linked and stiffer cortex (47,48) than interphase cells. We see net reduction in temporal fluctuations as captured by $SD_{(time)}$ (Fig. S13 *a*). Reduction of PSDs and $\overline{\sigma}$ (Fig. 5 *e*) is prominent at the lower frequencies. Both $SD_{(space)}$ and λ values are smaller than interphase cells (Figs. 5, *f* and *g* and S13 *a*). Cyto D treatment reduced the actin intensity at the cortex but does not result in cortex clearance as previously observed in interphase cells (Figs. 5 *b* and S13 *c*). We find a reduction of temporal fluctuations on Cyto D, Lat B, or blebbistatin (100 μM) treatment (Figs. 5, *d* and *e* and S13 *b*) in mitotic cells that resembles the response of pretreated interphase cells where cortex clearance is stopped. The blebbistatin (100 μM) here has a similar effect to that of blebbistatin (5 μM) on interphase cells. This is probably due to the increased myosin-II concentration in mitotic cells (49). The $SD_{(space)}$ increases on all treatments as seen in interphase cells (Fig. 5 *f*). In mitotic CHO cells, a similar trend of reduced temporal fluctuations is found. The $SD_{(space)}$ is already low for interphase CHO and therefore is not reduced any further (Fig. S13 *a*). Spatio-temporal fluctuations are, therefore, primarily reduced under mitosis.

To further explore systems in which the membrane can be debrided of its underlying cytoskeleton, we produce PMSs from CHO cells (Figs. 5 *c* and S14). We see reduced temporal fluctuations and spatial undulations (Figs. 5, *c–f* and S13 *d*) here. Although the mean relative height is lower for PMSs than the cells in the vicinity, for FBRs at similar mean relative heights (Fig. S13 *e*, *dotted line*) PMSs still display lower $SD_{(space)}$ than cells. A concomitant increase in λ (Fig. 5 *g*) with respect to live control cells suggests a more flattened membrane. The reduced fluctuations are in line with reports showing adhesion-based increase in lateral tension in liposomes (50).

So far, we have explored the averaged parameters of spatio-temporal fluctuations. Because heterogeneity is key to spatial segregation and regulation of activity at the plasma membrane, we next measured the spatial heterogeneity of temporal fluctuations.

Fluctuation maps reveal transient localized events creating heterogeneity

$SD_{(time)}$ maps (Fig. 2 *b*) show that fluctuations are nonuniform across the cell, but zooming into FBRs brings out the micron-sized heterogeneities (Fig. 2 *b*, *bottom*). We explored this by mapping $SD_{(time)}$ for a reduced time-interval (1 s) and capturing the evolution of fluctuations (Movie S4). In Fig. 6 *a*, we zoom into an FBR and highlight the transient nature of spatial heterogeneity of temporal fluctuations by following the formation and dissolution of a structure (*arrow*). These structures can appear and stay on for $\sim$1 s as depicted in the time evolution of line scans of $SD_{(time)}$ maps (Fig. 6, *b* and *c*). The timescales of appearance and disappearance of these features are $\sim$1.02 $\pm$ 0.79 and $\sim$0.79 $\pm$ 0.35 s, respectively (n = 20 events from a single cell). Such events (along with those not as clearly visible as the one in Fig. 6 *a*) are expected to increase the intra-FBR variation

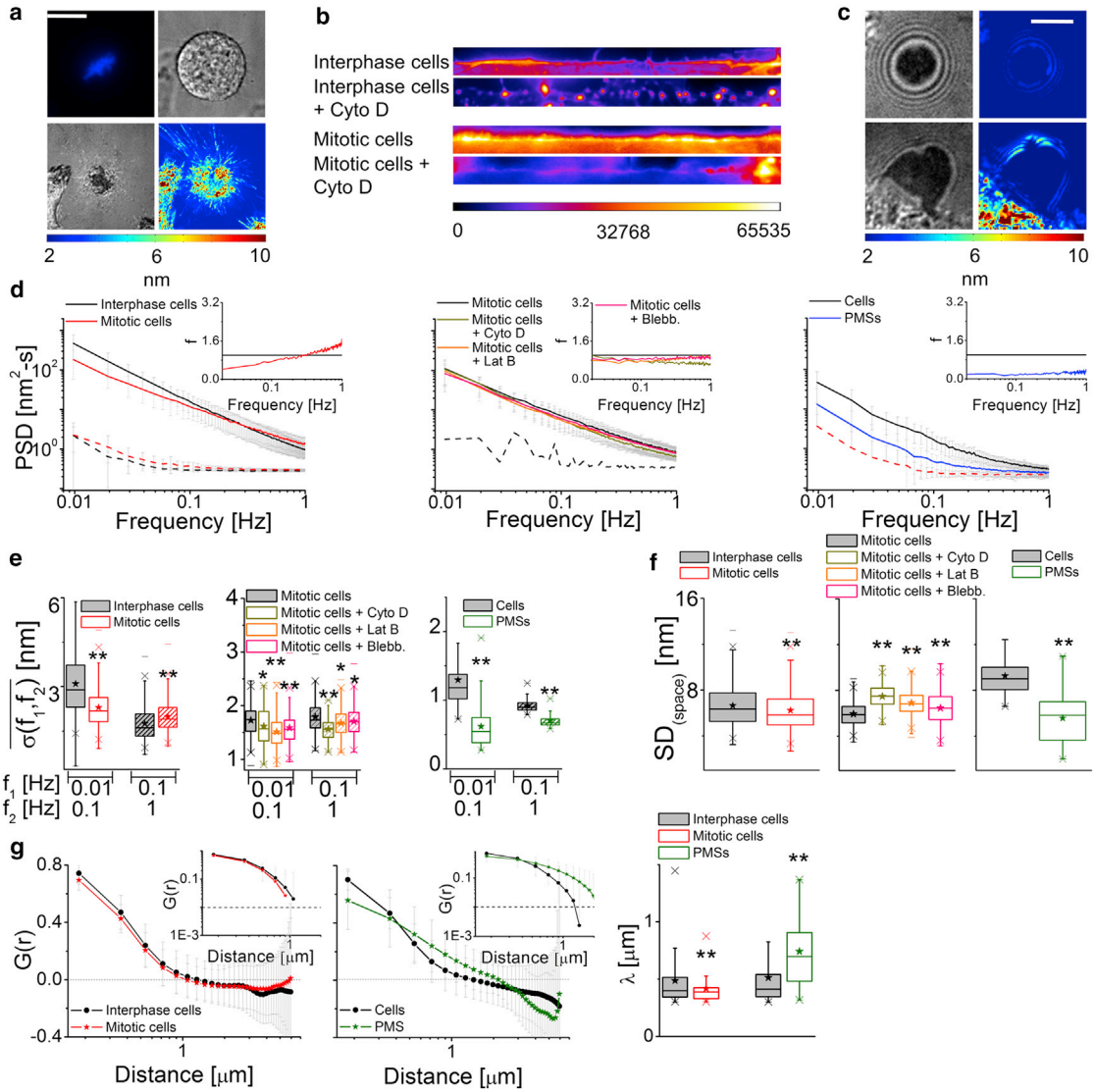

FIGURE 5 Membrane fluctuations in mitotic HeLa cells and in PMSs. (*a*) Mitotic HeLa cell is observed in fluorescence (*top left*) (DNA stained with Hoechst 33342), IRM (*bottom left*), and differential interference contrast (*top right*) modes along with the $SD_{(time)}$ map (*bottom right*). Scale bars, 10 μm. (*b*) Shown here is the linearized and color-coded cortex (60 μm × 9 μm) of actin-labeled interphase and mitotic cells in normal and Cyto D-treated conditions. (*c*) Given here are representative images of IRM (*left*) and $SD_{(time)}$ maps (*right*) of CHO-derived PMS (cell-free PMS (*top*), cell-attached PMS (*bottom*)). Scale bars, 5 μm. (*d*) Given here are PSDs for cells, PMSs (*solid lines*), and their backgrounds (*dashed lines*) with the insets showing the value *f*; (*left*) $N = 30$ cells each, $n_{interphase} = 639$ FBRs, and $n_{mitotic} = 352$ FBRs; (*middle*) $N = 15$ cells each, $n_{mitotic} = 105$ FBRs, $n_{mitotic\ +\ Cyto\ D} = 85$ FBRs, $n_{mitotic\ +\ Lat\ B} = 182$ FBRs, and $n_{mitotic\ +\ blebbistatin} = 215$ FBRs. (*Right*) Shown here is $N = 10$ cells/PMSs each, $n_{cell} = 70$ FBRs, and $n_{PMS} = 85$ FBRs. (*e* and *f*) The parameters of temporal fluctuations and spatial undulations of cells/PMSs are given in the mentioned conditions. *$p < 0.05$, **$p < 0.001$, one-way ANOVA. (*g*) Shown here are the averaged spatial ACFs (and their log-log plots, *top inset*) and correlation lengths ($n_{interphase} = 447$ FBRs, $n_{mitotic} = 199$ FBRs, $N = 50$ cells each; $n_{cells} = 130$ FBRs, $n_{PMS} = 39$ FBRs, and $N = 15$ cells/PMS). *$p < 0.05$, **$p < 0.001$, Mann-Whitney U test. See also Figs. S13 and S14; Tables S2 and S3. To see this figure in color, go online.

of $SD_{(time)}$ in the map. We hence calculate the $SD(SD_{(time)})$ for different conditions to quantify the short length-scale heterogeneity (Figs. 6, *d* and *e* and S15 *a*). We find that ATP depletion, mitosis, and Jas treatment reduce the heterogeneities, and the cortex disorganization by Cyto D/Lat B/blebbistatin (100 μM) increases them (Fig. 6 *e*; Table S2). Because a reduction in the basal (mean) $SD_{(time)}$ can also lower $SD(SD_{(time)})$, to normalize out the effect of the basal value we calculate $SD(SD_{(time)})/Mean(SD_{(time)})$ .The ratio obtained for all treatments is subtracted from that of the control set. Whereas we observe reduced values (Fig. S15 *b*) on treatments that affect cellular activity and on stabilized cortex (Jas), perturbations affecting the cytoskeleton either increase or do not change the short length-scale heterogeneities. At short length scales (<2 μm), therefore, cellular activity results in enhanced heterogeneities (Fig. S5 *d*; Supporting Discussion).

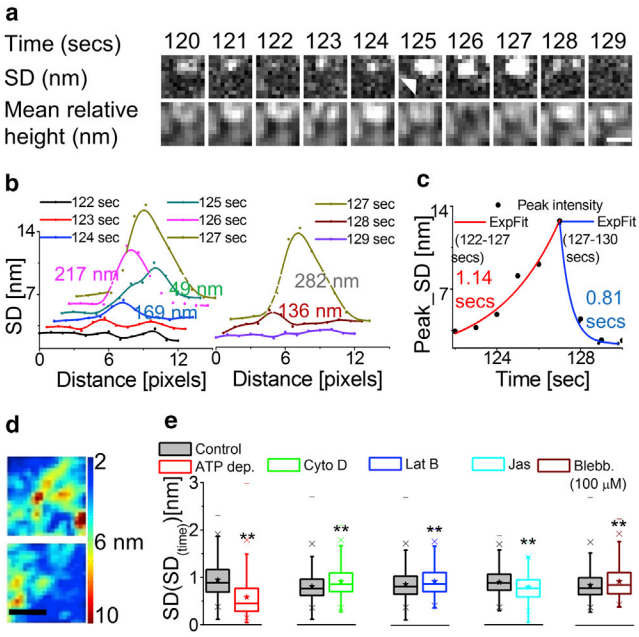

FIGURE 6 Characteristics of transient heterogeneities in fluctuations. (*a*) Given here is the $SD_{(time)}$ and mean relative height map of an FBR. Scale bars, 1 μm. (*b*) Shown here is a line scan of $SD_{(time)}$ across the feature (*white arrow*) at the mentioned time-points. The numbers mentioned are the SD of the Gaussian fits to profiles. (*c*) Variation of peak values of $SD_{(time)}$ are given at different time-points, exponential fits, and extracted timescales. (*d*) Given here are typical maps of $SD_{(time)}$ for a pair of FBRs. Scale bars, 1 μm. (*e*) Shown here is $SD(SD_{(time)})$ for different conditions (N = 30 cells each). $^{*}p < 0.05$ and $^{**}p < 0.001$, one-way ANOVA. See also Fig. S15; Tables S2 and S3. To see this figure in color, go online.

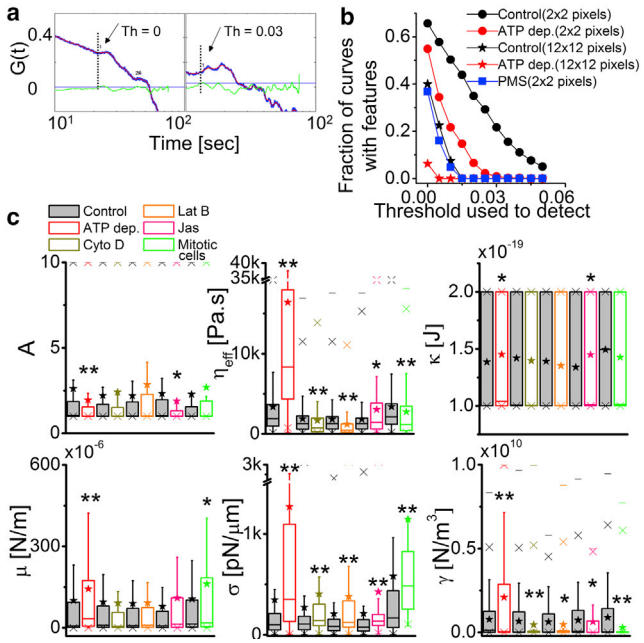

FIGURE 7 Local heterogeneities and underlying membrane mechanics. (*a*) Shown here are zoomed-in temporal ACFs (*blue*) and slopes (*green*) of smoothened ACFs (*red*). Horizontal lines denote the slope threshold (*Th*) set in each given to detect features (*arrow*). The vertical lines denote the crossovers. (*b*) Given here is the fraction of ACF curves with features obtained using different thresholds (N = 9 cells, $n_{control}$ = 3765 FBRs, $n_{ATP\ depletion}$ = 1987 FBRs; N = 10 PMSs, and n = 352 FBRs). (*c*) Membrane mechanical parameters A, η_{eff}, κ, μ, σ, and γ are obtained from fitting PSDs to a theoretical model ($n_{control}$ = 1238 FBRs, $n_{ATP\ depletion}$ = 811 FBRs, N = 80 cells each; $n_{control}$ = 595 FBRs, $n_{Cyto\ D}$ = 378 FBRs, N = 40 cells each): $n_{control}$ = 488 FBRs, $n_{Lat\ B}$ = 300 FBRs, N = 30 cells each; $n_{control}$ = 199 FBRs, n_{Jas} = 106 FBRs, N = 20 cells each; and $n_{interphase}$ = 329 FBRs, $n_{mitotic}$ = 101 FBRs, N = 30 cells each). $^{*}p < 0.05$, $^{**}p < 0.001$, Mann-Whitney U test. To see this figure in color, go online.

The range of timescales observed for the transient heterogeneities overlap with the range of τ (~0.2–2 s) underrepresented in ATP depletion cells (Fig. 3 *f*). We also find that the temporal ACFs display peaklike features (Fig. 2 *a*(*vi*), *arrow*) when averaged over 0.36 × 0.36 μm^2, which diminish on averaging over longer distances (Fig. 7, *a* and *b*). The steeper peaks are more frequent (in 21% ACFs) in control cells than in ATP depletion cells (in 8% ACFs), and rarely present in PMSs (Fig. 7 *b*). However, ATP depletion does not completely abrogate the features from the ACFs.

To understand if different amplitudes of fluctuations can coexist at distal (>2 μm) regions across the same cell, we compared percent dissimilarity as a measure of long-range heterogeneity. We see that ~60% FBR pairs are dissimilar in control cells (Fig. S15, *c* and *d*). This is reduced on fixation and ATP depletion followed by Cyto D, but there is no significant difference seen for any other treatments (Fig. S15, *c* and *d*; Table S2). The distinctly different fluctuations at distal FBRs may be caused due to short length-scale heterogeneities that are subdued but not abrogated in ATP depletion cells.

Hence, spatial mapping of temporal fluctuations reveals transient heterogeneities and shows that distal regions in the cell can have dissimilar fluctuations. We next compare the data with theoretical models to understand the underlying membrane mechanics.

Comparison with theoretical models

Fluctuations in RBCs have been compared in the literature with different models to extract membrane mechanical properties (16,32,35,51). These models either explicitly incorporate effect of direct forces on membranes or use equilibrium descriptions and account for active processes by an increase in the effective temperature. Because, in our data, bumps and peaks in the ACF (Fig. 2 *a*(*vi*))—signatures of active fluctuations—are no longer distinguishable when averaged over the whole FBR, we therefore do not use models describing direct effect of active forces. Instead, we fit the PSDs (averaged over FBRs) using a description (Eq. 1) that incorporates a higher effective temperature (or, active temperature A*T) to account for cellular activity (35). We also consider the contribution (16,35,51–53) of effective cytoplasmic viscosity (η_{eff}), bending rigidity (κ),

shear modulus (μ), membrane tension (σ), and confinement (γ). The PSDs are fit with the following equation:

$$PSD(f) = \frac{4\eta_{\mathrm{eff}} A k_{\mathrm{B}} T}{\pi} \int_{q_{\min}}^{q_{\max}} \frac{dq}{\left[4\eta_{\mathrm{eff}}(2\pi f)\right]^2 + \left[\kappa q^3 + \frac{9k_{\mathrm{B}}T}{16\pi\kappa}\mu q + \sigma q + \frac{\gamma}{q}\right]^2}. \quad (1)$$

Although other parameters fall in the expected range (Fig. 7 *c*), the η_{eff} has values much higher (~1500 Pa.s) than that of water or cytoplasm (54). However, micropipette aspiration experiments on fibroblasts (55) and simulations of the cross-linked actin-network (56) report similar values for η_{eff}, implying that the cortex contributes to η_{eff} due to slow relaxation times of the cross-linked actin network. This is supported by the observation (Fig. 7 *c*) that η_{eff} reduces on perturbing the actomyosin cytoskeleton with Cyto D or Lat B, but increases by the action of Jas as well as on ATP depletion.

Comparing the values of σ for control cells with those obtained from imaging studies (57) or tether-pulling experiments (58,59), we find the numbers to be in the right range (~10–450 pN/μm). No decrease of σ is seen when fluctuations are enhanced (for Cyto D, Lat B), but increased σ correlates with decreased fluctuations (in ATP depletion, Jas, and mitosis). Decreased A (ATP depletion and Jas) and increased κ/μ (ATP depletion, Jas/mitosis) correlate with decreased fluctuations. The γ-values decreased for all cytoskeletal perturbations as well for mitosis, but increased on ATP depletion. The γ-values did not fall below 10^8 N/m^3 on cytoskeleton disruption (Supporting Discussion), implying contributions from not just the cortex but also from other sources (confinement due to the coverslip).

DISCUSSION

Through implementation of IRM and image analysis, we successfully create spatial maps of the temporal fluctuations in three different cell lines. The study of membrane fluctuations in nucleated cells has been experimentally challenging (14) due to the complex internal architecture of cells. Firstly, because we do not use the absolute height and instead measure Δh—the variation of height in time or space—we could use beads-based calibration and avoid assumptions of internal refractive indices. Secondly, by stringently identifying pixels that remain FBRs throughout the time-lapse imaging, we hoped to have also eliminated regions where intensity reached values away from the first branch due to reflections from internal structures. Comparison with experimentally measured quantities reveal the measured amplitudes ($SD_{(\mathrm{time})}$, $SD_{(\mathrm{space})}$) to range from ~4–8 nm—similar to other reports in adherent nucleated cells (6,60). Incorporating dual wavelength imaging, in future, will add to the stringency of identification of FBRs.

The first striking observation is about the basal level of fluctuations. In the three cell lines we chose, epithelial-like (HeLa and CHO) and a myoblast cell line (C2C12), spectra of fluctuations are not significantly different. Mitotic cells, in contrast, displayed different characteristics from interphase cells. Whether this indicates regulation of fluctuations, such as membrane tension homeostasis (61), is a relevant future application of the technique.

Activity due to membrane proteins (36) or the underlying cytoskeleton has been reported to act as fluctuating force monopole/dipoles on the membrane, enhancing fluctuations (37,62). In our study, amplification of temporal fluctuations by cellular activity is observed to be true for all cells and cell lines used. Signatures of direct forces impacting fluctuations have been reported in RBCs and vesicles (16,36,37,62). In RBCs, analyzing temporal ACFs for different spatial modes have demonstrated forces acting at ~5×10^{-3} pN and ~0.1 s (16). In our system, ACFs of control cells display peaklike features (similar to active fluctuations in RBCs) as well as extra timescales (compared to ATP-depleted ones) that are in close range to timescales of transient heterogeneities observed. Various membrane activities occur in this range of timescales—membrane trafficking, blebbing, actin protrusions—which may be responsible for this effect. Although signatures exist, the clear demarcation of active fluctuations in cells needs measurement of their mechanical response.

The surprising part of the study is that cellular activity, which is expected to increase the dynamics of the system, flattens spatial undulations. It needs to be noted that decreased $SD_{(\mathrm{space})}$ and increased λ are signatures of membrane flattening. Because $SD_{(\mathrm{space})}$ and λ are calculated across an ~4 and 11 μm^2 area, respectively, with diffraction-limited lateral resolution, the flattening by activity reported here is at micrometer scales in contrast to the nanometer-scale temporal dynamics. This flattening is in line with reports that suggest that the contractile cytoskeleton creates coherence in the mechanical connectivity required for long-range (μm-scale) force transmission during cell spreading (63). Strong alterations to the

cortex (Cyto D/Lat B) or its dynamics (Jas, ATP depletion) both affect the parameters and support the role of cytoskeleton in flattening the undulations. Mitotic cells, owing to their limited adhesion and rounding at the edges ($\sim$6 μm apart), show decreased λ although the $SD_{(space)}$ is reduced.

The study also highlights the dual role of cortex in setting the fluctuations. Actin polymerization and myosin-II based activities can individually enhance fluctuations. However, the intact cortex dampens fluctuations and this reduction is not lost until the cortex is cleared, as seen both in interphase and mitotic cells. Other actin structures may have different contributions. Stress fibers (contributing 13 $\pm$ 10% actin at the basal cortex of interphase HeLa, measured over 25 cells, and absent in mitotic cells) do not qualitatively dominate over the impact of the cortex. Short actin filaments and their myosin-II based activity can enhance fluctuations. Slow and large actin waves (wavelength: $\sim$2 μm, speed: $\sim$20 nm/s, mostly reported at cell edges of spreading cells, and may also exist at the basal membrane (5,64)) are expected to cause low-frequency fluctuations (0.01 Hz). Although specific wavelike features are not observed in this study, the expected frequency range (0.01–0.03 Hz) shows (Fig. 4 *b*, *inset*) a relatively positive contribution to temporal fluctuations from the cortex. At a similar frequency range, mitotic cells also show reduced temporal fluctuations. Therefore, this frequency range has a contribution from actomyosin activity related to spread-out cells.

Comparing the PSDs with a theoretical description of fluctuating membranes adapted from existing models (16,32,35,51) suggests the possible mechanisms behind the effect of perturbing activity or the cytoskeleton. Most values and effect of drugs are close to expectations in comparison to reports/predictions in literature (Supporting Discussion). In general, we find that loss of activity leads to increase in tension, indicating an active softening of the membrane—also observed in RBCs (16,32,37,62). However, the amplification of fluctuations by activity is a combined effect of increase in active temperature, reduction of confinement, and a decrease in tension. The damping role of the cytoskeleton, on the other hand, appears to be arising due to increased confinement of the membrane. It needs to be noted that confinement may arise not only from the cortex but also from the coverslip. In mitotic cells, reduced fluctuations are found to correspond to increase in tension, and values (1146 $\pm$ 1770 pN/μm) are close to the surface tension reported in the literature (65).

Hence, by applying IRM, creating spatial maps of temporal fluctuations, and comparing with theoretical descriptions, we provide better understanding about the role of activity and cytoskeleton in setting up the state of fluctuations. We demonstrate that spatial undulations are actively diminished by the cytoskeleton whereas temporal fluctuations intricately depend on the details of the active state, cytoskeleton integrity, and contractility. Fluctuations display transient heterogeneities and long length-scale dissimilarity. The mechanical parameters extracted corroborate the interpretation of the measurements. The functional role of spatial heterogeneity observed in this study and the spatial mapping of corresponding mechanical parameters, especially through coupling of IRM to TIRF microscopy, need future investigation.

SUPPORTING MATERIAL

Supporting Discussion, fifteen figures, four tables, and four movies are available at http://www.biophysj.org/biophysj/supplemental/S0006-3495(17)30964-5.

AUTHOR CONTRIBUTIONS

B.S. conceptualized the project. B.S. and A.B. set up the system. A.B. performed and analyzed the experiments. B.S. and A.B. analyzed and interpreted the data. A.A. established and performed experiments with the PMSs. B.S. and A.B. wrote the article. All authors edited the article.

ACKNOWLEDGMENTS

We thank Rajesh Kumble Nayak for the code used for calculating the PSD, Kaushik Sengupta (Saha Institute of Nuclear Physics, Kolkata) for the C2C12 cells, Jayasri Das Sarma for HeLa cells, and Deepak Kumar Sinha (Indian Association of Cultivation of Sciences, Kolkata) for CHO cells and critical reading of the manuscript.

This work was supported by the Wellcome Trust/DBT India Alliance Fellowship (grant No. IA/I/13/1/500885) awarded to B.S.

REFERENCES

1. Zimmerberg, J., and M. M. Kozlov. 2006. How proteins produce cellular membrane curvature. *Nat. Rev. Mol. Cell Biol.* 7:9–19.
2. McMahon, H. T., and J. L. Gallop. 2005. Membrane curvature and mechanisms of dynamic cell membrane remodelling. *Nature.* 438:590–596.
3. Giannone, G., B. J. Dubin-Thaler, …, M. P. Sheetz. 2004. Periodic lamellipodial contractions correlate with rearward actin waves. *Cell.* 116:431–443.
4. Döbereiner, H.-G., B. J. Dubin-Thaler, …, M. P. Sheetz. 2006. Lateral membrane waves constitute a universal dynamic pattern of motile cells. *Phys. Rev. Lett.* 97:038102.
5. Chen, C.-H., F.-C. Tsai, …, C.-H. Lee. 2009. Three-dimensional characterization of active membrane waves on living cells. *Phys. Rev. Lett.* 103:238101.
6. Pierres, A., A. M. Benoliel, …, P. Bongrand. 2008. How cells tiptoe on adhesive surfaces before sticking. *Biophys. J.* 94:4114–4122.
7. Monzel, C., D. Schmidt, …, R. Merkel. 2015. Measuring fast stochastic displacements of bio-membranes with dynamic optical displacement spectroscopy. *Nat. Commun.* 6:8162.
8. Cardoso Dos Santos, M., R. Déturche, …, R. Jaffiol. 2016. Topography of cells revealed by variable-angle total internal reflection fluorescence microscopy. *Biophys. J.* 111:1316–1327.
9. Dubin-Thaler, B. J., G. Giannone, …, M. P. Sheetz. 2004. Nanometer analysis of cell spreading on matrix-coated surfaces reveals two distinct cell states and STEPs. *Biophys. J.* 86:1794–1806.

10. Pezeshkian, W., H. Gao, …, J. C. Shillcock. 2017. Mechanism of Shiga toxin clustering on membranes. *ACS Nano.* 11:314–324.
11. Fenz, S. F., T. Bihr, …, A.-S. Smith. 2017. Membrane fluctuations mediate lateral interaction between cadherin bonds. *Nat. Phys.*
12. Tarantola, M., E. Sunnick, …, A. Janshoff. 2011. Dynamic changes of acoustic load and complex impedance as reporters for the cytotoxicity of small molecule inhibitors. *Chem. Res. Toxicol.* 24:1494–1506.
13. Lo, C. M., C. R. Keese, and I. Giaever. 1993. Monitoring motion of confluent cells in tissue culture. *Exp. Cell Res.* 204:102–109.
14. Monzel, C., and K. Sengupta. 2016. Measuring shape fluctuations in biological membranes. *J. Phys. D Appl. Phys.* 49:243002.
15. Park, Y., C. A. Best, …, M. S. Feld. 2010. Metabolic remodeling of the human red blood cell membrane. *Proc. Natl. Acad. Sci. USA.* 107:1289–1294.
16. Rodríguez-García, R., I. López-Montero, …, F. Monroy. 2015. Direct cytoskeleton forces cause membrane softening in red blood cells. *Biophys. J.* 108:2794–2806.
17. Bereiter-Hahn, J., C. H. Fox, and B. Thorell. 1979. Quantitative reflection contrast microscopy of living cells. *J. Cell Biol.* 82:767–779.
18. Abercrombie, M., and G. A. Dunn. 1975. Adhesions of fibroblasts to substratum during contact inhibition observed by interference reflection microscopy. *Exp. Cell Res.* 92:57–62.
19. Curtis, A. S. G. 1964. The mechanism of adhesion of cells to glass. A study by interference reflection microscopy. *J. Cell Biol.* 20:199–215.
20. Godwin, S. L., M. Fletcher, and R. P. Burchard. 1989. Interference reflection microscopic study of sites of association between gliding bacteria and glass substrata. *J. Bacteriol.* 171:4589–4594.
21. Rädler, J. O., and E. Sackmann. 1993. Imaging optical thicknesses and separation distances of phospholipid vesicles at solid surfaces. *J. Phys. II.* 3:727–748.
22. Limozin, L., and K. Sengupta. 2009. Quantitative reflection interference contrast microscopy (RICM) in soft matter and cell adhesion. *ChemPhysChem.* 10:2752–2768.
23. Schmid, I., and K. M. Sakamoto. 2001. Analysis of DNA content and green fluorescent protein expression. *In* Current Protocols in Cytometry. John Wiley, Hoboken, NJ, pp. 7.16.1–7.16.10.
24. Yahara, I., F. Harada, …, S. Natori. 1982. Correlation between effects of 24 different cytochalasins on cellular structures and cellular events and those on actin in vitro. *J. Cell Biol.* 92:69–78.
25. Wakatsuki, T., B. Schwab, …, E. L. Elson. 2001. Effects of cytochalasin D and latrunculin B on mechanical properties of cells. *J. Cell Sci.* 114:1025–1036.
26. Kovács, M., J. Tóth, …, J. R. Sellers. 2004. Mechanism of blebbistatin inhibition of myosin II. *J. Biol. Chem.* 279:35557–35563.
27. Bubb, M. R., I. Spector, …, K. M. Fosen. 2000. Effects of jasplakinolide on the kinetics of actin polymerization. An explanation for certain in vivo observations. *J. Biol. Chem.* 275:5163–5170.
28. Renard, H.-F., M. Simunovic, …, L. Johannes. 2015. Endophilin-A2 functions in membrane scission in clathrin-independent endocytosis. *Nature.* 517:493–496.
29. Beach, J. R., L. S. Licate, …, T. T. Egelhoff. 2011. Analysis of the role of Ser^{1}/Ser^{2}/Thr^{9} phosphorylation on myosin II assembly and function in live cells. *BMC Cell Biol.* 12:52.
30. Carpi, N., M. Piel, …, J. Fink. 2011. Micropatterning on glass with deep UV. *Protoc. Exch.*
31. Campillo, C., P. Sens, …, C. Sykes. 2013. Unexpected membrane dynamics unveiled by membrane nanotube extrusion. *Biophys. J.* 104:1248–1256.
32. Betz, T., M. Lenz, …, C. Sykes. 2009. ATP-dependent mechanics of red blood cells. *Proc. Natl. Acad. Sci. USA.* 106:15320–15325.
33. Alert, R., J. Casademunt, …, P. Sens. 2015. Model for probing membrane-cortex adhesion by micropipette aspiration and fluctuation spectroscopy. *Biophys. J.* 108:1878–1886.
34. Brochard, F., and J. F. Lennon. 1975. Frequency spectrum of the flicker phenomenon in erythrocytes. *J. Phys.* 36:1035–1047.
35. Gov, N., A. G. Zilman, and S. Safran. 2003. Cytoskeleton confinement and tension of red blood cell membranes. *Phys. Rev. Lett.* 90:228101.
36. Girard, P., J. Prost, and P. Bassereau. 2005. Passive or active fluctuations in membranes containing proteins. *Phys. Rev. Lett.* 94:088102.
37. Turlier, H., D. A. Fedosov, …, T. Betz. 2016. Equilibrium physics breakdown reveals the active nature of red blood cell flickering. *Nat. Phys.* 12:513–520.
38. Fodor, É., M. Guo, …, F. van Wijland. 2015. Activity driven fluctuations in living cells. *EuroPhys. Lett.* 110:48005..
39. Guo, M., A. J. Ehrlicher, …, D. A. Weitz. 2014. Probing the stochastic, motor-driven properties of the cytoplasm using force spectrum microscopy. *Cell.* 158:822–832.
40. Fakhri, N., A. D. Wessel, …, C. F. Schmidt. 2014. High-resolution mapping of intracellular fluctuations using carbon nanotubes. *Science.* 344:1031–1035.
41. Bretscher, A., K. Edwards, and R. G. Fehon. 2002. ERM proteins and Merlin: integrators at the cell cortex. *Nat. Rev. Mol. Cell Biol.* 3:586–599.
42. Fehon, R. G., A. I. McClatchey, and A. Bretscher. 2010. Organizing the cell cortex: the role of ERM proteins. *Nat. Rev. Mol. Cell Biol.* 11:276–287.
43. Dmitrieff, S., and F. Nédélec. 2016. Amplification of actin polymerization forces. *J. Cell Biol.* 212:763–766.
44. Gowrishankar, K., S. Ghosh, …, M. Rao. 2012. Active remodeling of cortical actin regulates spatiotemporal organization of cell surface molecules. *Cell.* 149:1353–1367.
45. Schliwa, M. 1982. Action of cytochalasin D on cytoskeletal networks. *J. Cell Biol.* 92:79–91.
46. Raucher, D., and M. P. Sheetz. 1999. Membrane expansion increases endocytosis rate during mitosis. *J. Cell Biol.* 144:497–506.
47. Neisch, A., and R. G. Fehon. 2008. FERMing up the plasma membrane. *Dev. Cell.* 14:154–156.
48. Kunda, P., A. E. Pelling, …, B. Baum. 2008. Moesin controls cortical rigidity, cell rounding, and spindle morphogenesis during mitosis. *Curr. Biol.* 18:91–101.
49. Ramanathan, S. P., J. Helenius, …, D. J. Muller. 2015. Cdk1-dependent mitotic enrichment of cortical myosin II promotes cell rounding against confinement. *Nat. Cell Biol.* 17:148–159.
50. Murrell, M. P., R. Voituriez, …, M. L. Gardel. 2014. Liposome adhesion generates traction stress. *Nat. Phys.* 10:163–169.
51. Gov, N., and S. A. Safran. 2005. Red blood cell shape and fluctuations: cytoskeleton confinement and ATP activity. *J. Biol. Phys.* 31:453–464.
52. Helfrich, W. 1973. Elastic properties of lipid bilayers: theory and possible experiments. *Z. Naturforsch. C.* 28:693–703.
53. Betz, T., and C. Sykes. 2012. Time resolved membrane fluctuation spectroscopy. *Soft Matter.* 8:5317–5326.
54. Bicknese, S., N. Periasamy, …, A. S. Verkman. 1993. Cytoplasmic viscosity near the cell plasma membrane: measurement by evanescent field frequency-domain microfluorimetry. *Biophys. J.* 65:1272–1282.
55. Thoumine, O., O. Cardoso, and J.-J. Meister. 1999. Changes in the mechanical properties of fibroblasts during spreading: a micromanipulation study. *Eur. Biophys. J.* 28:222–234.
56. Kim, T., M. L. Gardel, and E. Munro. 2014. Determinants of fluidlike behavior and effective viscosity in cross-linked actin networks. *Biophys. J.* 106:526–534.
57. Peukes, J., and T. Betz. 2014. Direct measurement of the cortical tension during the growth of membrane blebs. *Biophys. J.* 107:1810–1820.
58. Lieber, A. D., S. Yehudai-Resheff, …, K. Keren. 2013. Membrane tension in rapidly moving cells is determined by cytoskeletal forces. *Curr. Biol.* 23:1409–1417.
59. Sens, P., and J. Plastino. 2015. Membrane tension and cytoskeleton organization in cell motility. *J. Phys. Condens. Matter.* 27:273103.

60. Brodovitch, A., L. Limozin, …, A. Pierres. 2015. Use of TIRF to monitor T-lymphocyte membrane dynamics with submicrometer and subsecond resolution. *Cell. Mol. Bioeng.* 8:178–186.

61. Morris, C. E., and U. Homann. 2001. Cell surface area regulation and membrane tension. *J. Membr. Biol.* 179:79–102.

62. Gov, N. 2004. Membrane undulations driven by force fluctuations of active proteins. *Phys. Rev. Lett.* 93:268104.

63. Cai, Y., O. Rossier, …, M. P. Sheetz. 2010. Cytoskeletal coherence requires myosin-IIA contractility. *J. Cell Sci.* 123:413–423.

64. Gov, N. S., and A. Gopinathan. 2006. Dynamics of membranes driven by actin polymerization. *Biophys. J.* 90:454–469.

65. Fischer-Friedrich, E., A. A. Hyman, …, J. Helenius. 2014. Quantification of surface tension and internal pressure generated by single mitotic cells. *Sci. Rep.* 4:6213.

Biophysical Journal, Volume *113*

Supplemental Information

Mapping Cell Membrane Fluctuations Reveals Their Active Regulation and Transient Heterogeneities

Arikta Biswas, Amal Alex, and Bidisha Sinha

Supplemental Information

Mapping Cell Membrane Fluctuations Reveals Their Active Regulation and Transient Heterogeneities.

Arikta Biswas, Amal Alex[#] and Bidisha Sinha[*]

Dept. of Biological Sciences, Indian Institute of Science Education and Research (IISER) Kolkata, Mohanpur - 741246, West Bengal, India

[#] Present address: Dept. of Mechanistic Cell Biology, Max Planck Institute of Molecular Physiology, 44227 Dortmund, North Rhine-Westphalia, Germany

[*] Corresponding author (email- bidisha.sinha@iiserkol.ac.in)

Table of Contents

Supporting Discussion

1. Method of calibration with beads
    a. Adherent polystyrene beads (60 µm in diameter) are imaged in the IRM mode at EM 30 and varying exposure times.
    b. Linear ROIs are drawn on the bead radially outward from the centre using ImageJ and the intensities along the lines are plotted (Fig. 1 b, *top*). Intensity vs. height plots (Fig. 1 b, *bottom*) are also plotted by converting from radial distance (x) to height (h) by

    $$h - h_0 = R - \sqrt{R^2 - x^2} \qquad \text{Eq. (1)}$$

    where, R is the radius of the bead used and h_0 is the minimum separation distance (unknown) between the bead and the substrate.
    c. From the first branch of the intensity–height profile (Fig. 1 b, *bottom*), the maximum and minimum intensity of the first branch (I_{max}, I_{min}) and the S/2 (= (I_{max}+ I_{min})/2) are plotted with the varying exposure times and fitted linearly (Fig. 1 c, *top*).
    d. The slope of the first branch is also plotted with the varying exposure times for all the line profiles (Fig. 1 c, *bottom*).
    e. Next, cells are imaged in IRM keeping exposure time fixed at 50 ms (Fig. S1 a). To obtain the cell's I_{max}, the whole cell is manually searched for pixels with high intensity values (avoiding the nucleus) (Fig. S1 a, *right*). Such maximum intensity pixels lying close (within 15 x 15 pixels) to minimas (such that when connected by a line do not cross any other maxima, Fig. S1 b) are noted down, averaged and termed as I_{max}.
    f. The cell's S/2 is calculated from the IRM images of the cell by three methods
        i. Method 1: The I_{max} and I_{min} obtained from line scans (Fig. S1 a, *right*, Fig. S1 b) are used to calculate $S/2_{method\ 1}$ ((I_{max}+I_{min}) /2).
        ii. Method 2: Large 70 x 70 pixels regions are selected inside the cell (avoiding the nucleus) (Fig. S1 a) and the mean intensity from such regions are measured as $S/2_{method2}$.
        iii. Method 3: Large 50 x 50 pixels regions are selected outside the cell (Fig. S1 a) and the mean intensity from such regions are measured as $S/2_{method3}$.

Note that the measurement/calculation of the S/2 is done in more than 20 cells in each day. It is seen that the values of S/2 calculated from the three methods are similar to each other.

Henceforth, the third method is employed for analysis since it doesn't require the actual I_{min} to be attained at any point in the cell by close attachment of the membrane to substrate.

g. The value of S/2 obtained from the cell is used to identify the exposure time at which the bead is expected to have the same value of S/2. The exposure time is noted and I_{max}, I_{min} and slope ($\Delta I/\Delta h$) of the bead at the same exposure time is read out from the respective plots (Fig. 1 c). All the three methods used for obtaining the cell's S/2 are seen to be well correlated with that of the bead (Fig. S1 c)

h. The corresponding D (= $2I_{max} - S$) is next calculated (Table S1).

i. The values of the I_{max}, S/2 and D are compared between the cell (Table S1) and the bead and is seen to be within an error of 10% from each other.

We next justify that if the bead profile has the same D, slope of intensity-height profiles of beads can indeed be used for converting ΔI to Δh in cells though their reflectivities differ.

2. Justification of method of calibration.

The interference due to the reflection off the surface of the bead can be described theoretically as (1):

$$I = I_1 + I_2 + 2\sqrt{I_1 I_2}\cos[2kh(x,y) + \phi] \qquad \text{Eq. (2)}$$

where a monochromatic incident ray I_0 is first reflected at the glass-medium interface (refractive indices, n_0 and n_1 respectively, Fig. S1 d) to give ray I_1 which is further reflected at the medium-bead interface to give rise to ray I_2 with $k = \frac{2\pi n_1}{\lambda}$ and ϕ is a phase shift usually equal to π. $h(x,y)$ is the distance between the bead and the glass substrate at lateral position (x,y), λ is the wavelength of the light used and $I_1 = r^2_{01}I_0$, $I_2 = (1-r^2_{01})r^2_{12}I_0$ with Fresnel reflection coefficient $r_{ij} = \frac{n_i - n_j}{n_i + n_j}$ (i,j = 0,1,2).

Eq. (2) can be simplified and re-written as

$$2I = S - Dcos[2kh] \quad \text{Eq. (3)}$$

where $S = I_{max} + I_{min}$ and $D = I_{max} - I_{min}$ when $I_{max} = I_1 + I_2 + 2\sqrt{I_1 I_2}$ and $I_{min} = I_1 + I_2 - 2\sqrt{I_1 I_2}$.

However, reflections from the cell membrane can be due to multiple interfaces in contrast to the bead's single interface (Fig. S1 d). In such cases, the intensity vs. height profile is expected to be described by (1):

$$2I = S - 2Dcos\{2k[h(x,y) - h_0]\} \quad \text{Eq. (4)}$$

where $h_0 = -\frac{\lambda}{4\pi n_1} arctan \frac{\gamma sin\delta}{1+\gamma sin\delta}$, with $\gamma = \frac{r_{23}}{r_{12}}(1 - r_{12}^2)$, $\delta = \frac{4\pi n_2 d}{\lambda}$ and d is the membrane thickness of index n_2.

Fig. S1 d plots both Eq. 3 (single interface) and Eq. 4 (multiple interfaces) as well as the corresponding linear fits to the central part of the first branch. As observed though the profiles do not match, the slopes are equal (single interface: 0.01182 ± 1.44E-4; multiple interface: 0.0119 ± 1.43E-4). Therefore, the using of slope of the linear part of the intensity vs. height profile from the bead for ΔI to Δh conversion for cells is justified.

However, it is also evident, and must be noted, that the bead profile cannot be used for measuring the absolute height of the cell membrane.

Since the I_{max}, S/2 and D between the cell and the bead are strongly correlated (Fig. 1 e), for the next part – identification of FBRs in the cell, I_{max} and I_{min} of the bead (imaged on the same day) are used.

3. Method of identifying FBRs
    a. Exclude minimas and maximas
        i. Using Image J, for each pixel, the minimum and maximum intensity reached in the 2048 frames captured is found out and the new images are called the minima and maxima projection respectively.
        ii. A threshold is applied on the minima projection to keep only pixels with intensities ranging from I_{min} to I_{min} + 2000. These pixels have been represented in red in Fig.1 g.
        iii. A threshold is applied on the maxima projection to keep only pixels with intensities ranging from I_{max} - 2000 to 65500. These pixels have been represented in green in Fig. 1 g.

iv. A composite image is constructed by merging the thresholded projections as represented by Fig. 1 g.

b. Manual drawing of FBRs

i. Regions close (1-pixel distance) to red pixels (avoiding the cell nucleus) are selected and square ROIs (12x12 pixels) drawn avoiding any overlap with green pixels (Fig. 1 g).

4. Justification of method to identify FBRs:

The use of minima and maxima projections ensures that a pixel is assigned to be in the first branch only if its intensity never crosses or reaches the I_{min} and I_{max} throughout the time lapse imaging. Additionally, we use the fact that if we draw a line between a red pixel and a pixel at heights above 100 nm (second branch or higher), the line would traverse intermediate heights and therefore some pixels on the line must reach intensity I_{max} of the first branch. To elaborate, a height profile of such a line on the cell is simulated (Fig. S1 f) with the height spacing between adjacent pixels as 2 nm. This is because we calculated height spacing between adjacent pixels in HeLa cells to be ~ 1.9 ± 0.6 nm (from 140 μm^2 in FBRs of a cell, as in Fig. 1 i). The bead's Intensity-Height profile (Fig. 1 b, *bottom*) next is used to read out the corresponding intensities and the resulting intensity plot shows the expected crossing through I_{max} (marked out by red arrow).

In our identification of FBRs, we hence do not include pixels which when joined to the nearest minima (red pixels) by a line pass over maximas (green pixels).

5. Check for signatures of active fluctuations in our measurements:

The following three approaches are undertaken:

A) In brief, the temporal ACFs in the FBRs of the cell frequently displayed "bumps" or "peaks". For quantifying the frequency of occurrence of these features we proceed as follows. The ACF (Figs. 2 a(vi) and 7 a, blue line) is first smoothened using Savitzky-Golay filter (Fig. 7 a, red line) and the slope or spatial derivative is calculated, smoothened and rescaled (30x fold) for visualization on the same plot (Fig. 7 a, green line).

In the absence of bumps, the slope of the ACF has a negative value which monotonically increases with time. For forming features resembling bumps or

peaks the ACF curve first flattens or the slope becomes zero (Fig. 7 a, dashed line) before further increasing. The crossing of zero (or higher threshold values (Th)) by the slope (Fig. 7 a, green line) is computed. Such crossovers located before the intersection of the ACF with the x-axis are considered to represent "bumps" or "peak". ACF curves with at least one such feature is counted and the ratio of the number of such curves over the total number of curves analyzed is computed and plotted (Fig. 7 b).

Note that increasing Th (from left to right) allows features with increasingly steeper slopes to be chosen (Fig. 7 b). As depicted in Fig. 7 b, with respect to Control cells, in ATP depleted cells the probability of finding steeper features is substantially diminished. In PMS, even lesser fraction of curves is seen to have these features. Averaging ACFs across 12x12 pixels drastically reduces the probability of finding peaks even for Control cells (Fig. 7 b). We believe this implies that the features resembling bumps/peaks may be caused by local cellular activity.

B) We next checked for the existence of any extra timescales in the ACF due to activity that are not necessarily reflected as bumps/peaks. We therefore fitted individual ACFs with a three-term multi-exponential function. Though the sharper peaks cannot be fit the baseline can be captured (Fig. 2 a(vi), solid lines). We collate the timescales and amplitudes from >1900 fits, plot the distribution of timescales weighted with their corresponding amplitudes (Fig. 3 f). On comparing the distributions among the three sets, we find that Control cells have a higher probability of having timescales ranging from 0.2-2.2 sec (Fig. 3 f, black arrow) than ATP depleted cells or PMS. This range overlaps (although having an appreciable spread) with the timescales of events of heterogeneity observed previously (Fig. 6, main text).

We believe that the smaller (<0.1sec) timescales in the distribution originate from thermal motion of the membrane and the larger (>10sec) timescales reflect the slow active/passive relaxation.

C) We also checked the effect of activity on the nature of fluctuations by analysing the height distribution at every pixel. It is reported previously (2), that activity can result in non-Gaussian nature of fluctuations. We check for the normality of the height fluctuations for every pixel using the Kolmogorov-Smirnov hypothesis testing and map the corresponding p values. We observe that the p-values vary non-uniformly across the cell. The background fluctuations are Gaussian (high p value) while

pixels inside the cell have a higher probability to be non-Gaussian (p-value < 0.05). The numbers of pixels with non-Gaussian distributions reduce on ATP depletion which when averaged over FBRs (Fig. 3 g) show significant difference from the control. Therefore, our results indicate that ATP dependent activities lead to non-Gaussian fluctuations in the cell membrane.

From these results, we conclude that the signatures of active fluctuations are very local and not evident on averaging across a length scale of 2.16x2.16 μm^2.

6. Fitting of the PSD to a model

We have fitted our PSD(f) with a model.

$$S(f) = \frac{4\eta_{eff} A k_B T}{\pi} \int_{q_{min}}^{q_{max}} \frac{dq}{(4\eta_{eff}(2\pi f))^2 + \left[\kappa q^3 + \frac{9k_B T}{16\pi\kappa}\mu q + \sigma q + \frac{\gamma}{q}\right]^2} \quad \text{Eq. (5)}$$

that is a modified version of (3) and includes the parameters –active temperature (A*T), effective viscosity (η_{eff}), bending rigidity (κ), shear modulus (μ), membrane tension (σ) and confinement (γ) as presented in Fig. 7 c. The fitting is performed using MATLAB and fits with $R^2 > 0.9$ are considered.

The PSDs used for fitting are averaged over single FBRs. It is important to note that the bumps and peaks in the ACF (Fig. 2 a(vi)) are no longer distinguishable when averaged over the whole FBR (12x12 pixels = 2.16 µm x 2.16 µm) (Fig. 7 b). We therefore feel it is justified to use the model in comparison to models where the passive thermal motion as well as contributions from active forces are considered (3). In our case the parameter A (in active temperature A*T) is used to capture the effect of activity (4). From the PSD fits, we obtained a distribution of parameter values (of A, η_{eff}, κ, μ, σ, and γ) as presented in Fig. 7 c. While other parameters fall in the expected range, the η_{eff} has values much higher (~1000 Pa-sec) than that of water or cytoplasm (0.001-0.01 Pa-sec (5)). We propose the acto-myosin cytoskeleton contributes to the η_{eff} due to the slow relaxation times of the crosslinked actin network. This is supported by the observation (Fig. 7 c) that η_{eff} reduces on perturbing the acto-myosin cytoskeleton with Cyto D or Lat B but increases by the action of Jas as well as on ATP depletion. The values of η_{eff} are also close to predictions from numerical/theoretical estimates (6).

The parameter A which indicates the degree of contribution of active motions decreases on ATP depletion (from 2.6 to 2) and on Jas treatment (from 2.3 to 1.9). The other treatments do not show in any significant change in the values of A from their respective controls. In RBCs, ATP depletion has been shown to reduce A from 3 to 1 (7).

ATP depletion in this study also leads to increase in κ, μ, σ - as observed in RBCs (3, 8). κ decreases (not significant) on Cyto D or Lat B but increases (significant) on Jas treatment. μ decreases on Cyto D and Lat B and increases on Jas treatment – though the changes are statistically not significant.

The increase in membrane tension (σ) is also seen when the cytoskeleton is perturbed by Cyto D, Lat B, or Jas. Interestingly, in RBCs too, all cytoskeletal or metabolic perturbations have been observed to lead to an increase in tension. Cytoskeleton activity and its mechanical coupling is believed to lead to softening of the membrane (3). In adherent nucleated cells, the presence of endomembrane and the cytoskeleton/ATP dependent trafficking rates need to be investigated separately in future to understand the implication of the rise in tension. Comparing the values of σ for control cells with those obtained from imaging studies (9) or tether–pulling experiments (10), we find the numbers to be in the right range (~10-450 pN/μm).

We find that the confinement parameter γ to be in the right order of magnitude (10^8-10^{10}) as predicted (4) for RBCs (10^8 J/m^4). We expect the confinement to arise from the cytoskeleton as well as connections with the ECM/ confinement due to the coverslip. We find γ to increase on ATP depletion but decrease on Cyto D, Lat B treatments. However, the γ values do not drop below 10^8 which implies the contribution of other sources. Surprisingly Jas treatments also result in reduction of γ and hence we believe that γ is not solely dependent on the presence of intact cytoskeleton.

Finally, the fits also show that the tension in mitotic cells is higher from the interphase cells as is seen in literature (11). Among the other parameters a significant increase in μ along with a significant decrease in η_{eff}, γ is seen in mitotic cells.

Table S1

Day	Cell				Bead				ΔI/Δh
	I_{min} (au)	I_{max} (au)	S/2 (au)	D (au)	I_{min} (au)	I_{max} (au)	S/2 (au)	D (au)	
1	20052 ± 2691	46461 ± 2333	33256 ± 527	26410 ± 3561	19309 ± 157	47203 ± 2147	33256 ± 1106	27895 ± 2152	320
2	20791 ± 3246	46505 ± 2090	33648 ± 694	25714 ± 4359	18960 ± 155	46335 ± 2123	32648 ± 1094	27376 ± 2129	320
3	21454 ± 2678	45407 ± 2778	33431 ± 857	23954 ± 3858	19409 ± 157	47452 ± 2153	33430 ± 1109	28044 ± 2159	320
4	12652 ± 2740	34123 ± 2201	23387 ± 912	21472 ± 3514	13196 ± 336	33576 ± 888	23386 ± 577	20381 ± 949	290
5	27175 ± 2099	45242 ± 1829	36208 ± 1263	18068 ± 2784	25498 ± 1055	46916 ± 2264	36207 ± 1599	21418 ± 2498	210
6	22326 ± 2990	42481 ± 1820	32403 ± 908	20155 ± 3500	22404 ± 243	42404 ± 901	32404 ± 493	20001 ± 933	200
7	8079 ± 1355	16665 ± 1092	12372 ± 465	8586 ± 1740	8447 ± 41	16298 ± 210	12372 ± 103	7852 ± 214	94
8	9669 ± 1042	16769 ± 801	13219 ± 312	7101 ± 1314	9125 ± 46	17312 ± 179	13219 ± 89	8188 ± 185	90
9	8128 ± 1173	15782 ± 1027	11955 ± 268	7654 ± 1559	8071 ± 106	15839 ± 553	11955 ± 303	7768 ± 563	90
10	9094 ± 15054	19709 ± 1451	14402 ± 260	10616 ± 2090	8429 ± 99	20375 ± 399	14402 ± 198	11947 ± 411	130
11	7804 ± 1263	17396 ± 1096	12600 ± 469	9593 ± 1672	7170 ± 73	18030 ± 627	12600 ± 286	10861 ± 631	100
12	6551 ± 1209	17900 ± 1267	12225 ± 362	11349 ± 1751	8025 ± 166	16425 ± 312	12225 ± 222	8400 ± 353	82
13	5779 ± 998	13130 ± 935	9455 ± 299	7352 ± 1367	6727 ± 73	12181 ± 156	9454 ± 98	5455 ± 173	80
14	13855 ± 1538	28868 ± 1629	21362 ± 462	15014 ± 2240	12481 ± 137	30246 ± 245	21363 ± 119	17765 ± 280	189
15	11983 ± 1449	28189 ± 1457	20086 ± 395	16206 ± 2055	10625 ± 71	29546 ± 210	20086 ± 110	18922 ± 221	215
16	7177 ± 1418	18173 ± 1196	12675 ± 385	10996 ± 1855	7392 ± 182	17958 ± 2032	12675 ± 1021	10566 ± 2040	108
17	5546 ± 1066	16925 ± 1012	11235 ± 157	11379 ± 1470	6620 ± 74	15850 ± 583	11235 ± 292	9230 ± 588	119
18	6562 ± 846	15216 ± 821	10889 ± 188	8654 ± 1179	5614 ± 278	16164 ± 1381	10889 ± 818	10551 ± 1408	119
19	5804 ± 1192	15549 ± 1148	10677 ± 158	9745 ±1655	5514 ± 73	15840 ± 244	10677 ± 134	10326 ± 254	116
20	6270 ±897	13838 ± 815	10054 ± 269	7569 ± 1212	5821 ± 51	14289 ± 318	10055 ± 169	8468 ± 322	102

Values of the calibration used for analysis

Values of I_{max}, I_{min}, S/2 and D for cells and beads on different days and corresponding ΔI/Δh conversions used for analysis. Details in Supporting Discussion.

Figure S1

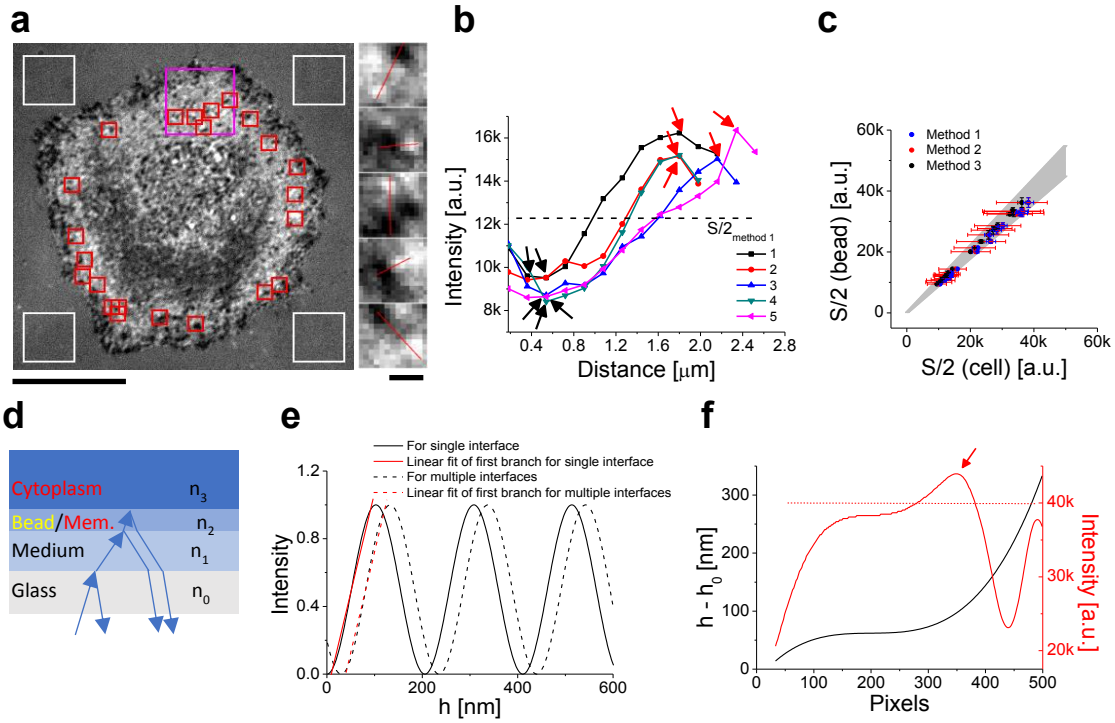

Figure S1. Justification of calibration with beads.

(a) Left: A representative IRM image of a HeLa cell with ROIs marked in red, magenta and white to calculate S/2 by methods 1, 2 and 3 (see Supporting Discussion) respectively. Scale bar: 10 μm. Right: Zoomed-in views of five FBRs with lines in red passing between minimas and maximas. Scale bar: 1 μm. (b) Profiles of lines shown in right panel of (a). Red and black arrows mark out I_{max} and I_{min} respectively and the dashed line represents $S/2_{method\ 1}$. (c) A comparison of S/2 in beads and cells (by the three methods), N = 20 days. Grey region covers $y = x \pm 0.1\ x$. (d) A schematic diagram of rays traversing through glass-medium and a single interface at the object's surface (marked as bead in yellow, relevant interfaces n_0-n_2) or multiple interfaces due to the presence of membrane as well as cytoplasm (marked in red, relevant indices n_0-n_3). (e) A comparison of simulated intensity vs. height profiles of interferences due to single and multiple interfaces with first branch fitted to a line. (f) Simulation of height and intensity for a cell with ~ 2 nm as the height spacing between two pixels. Arrow shows the I_{max} and the dotted line denotes $I_{max} - 2000$ which is used for thresholding.

Figure S2

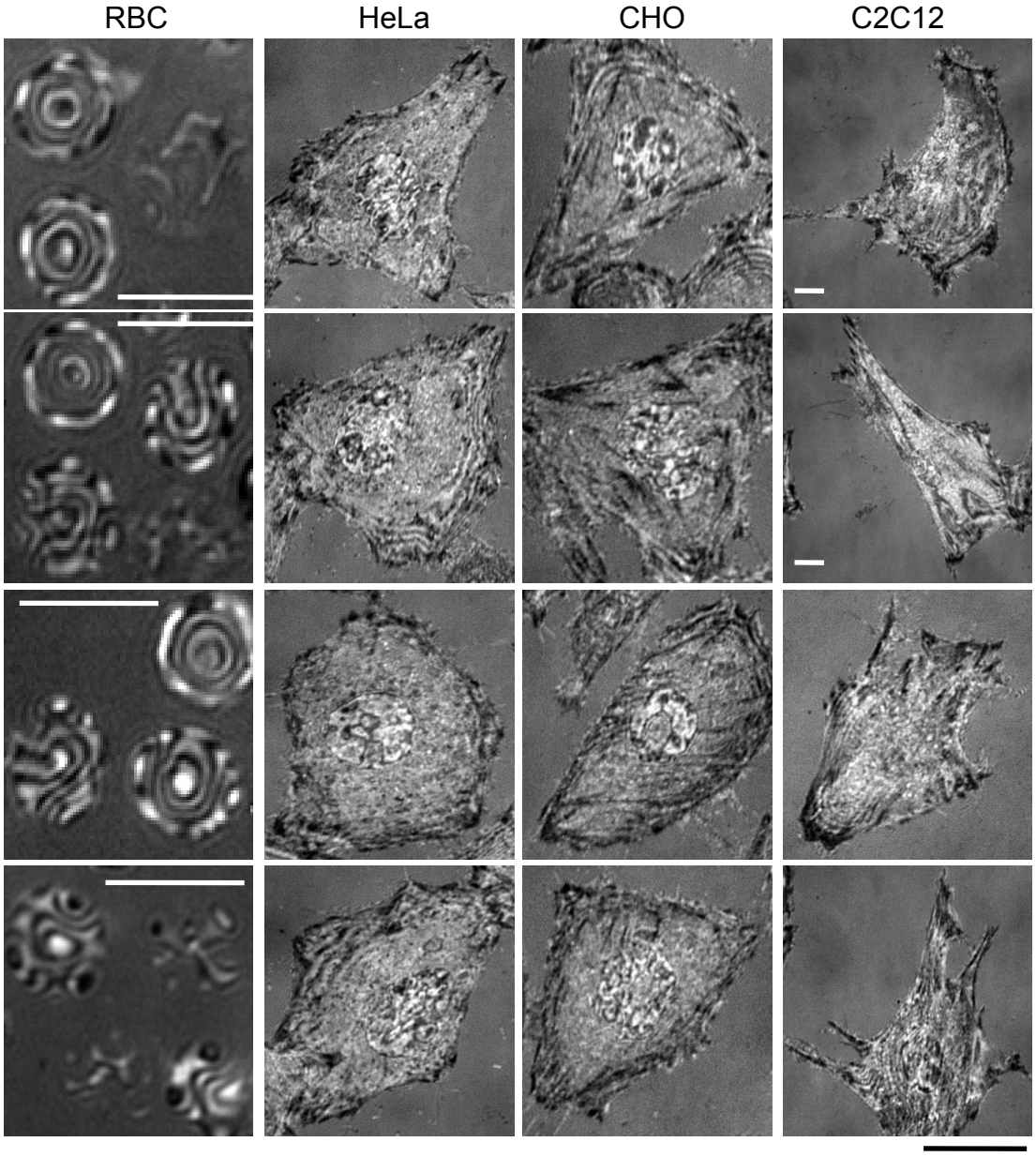

Figure S2. IRM shows heterogeneous membrane topology in cells.

Representative IRM images of adhered RBC, HeLa, CHO and C2C12 cells. Scale bar: 10 μm.

Figure S3

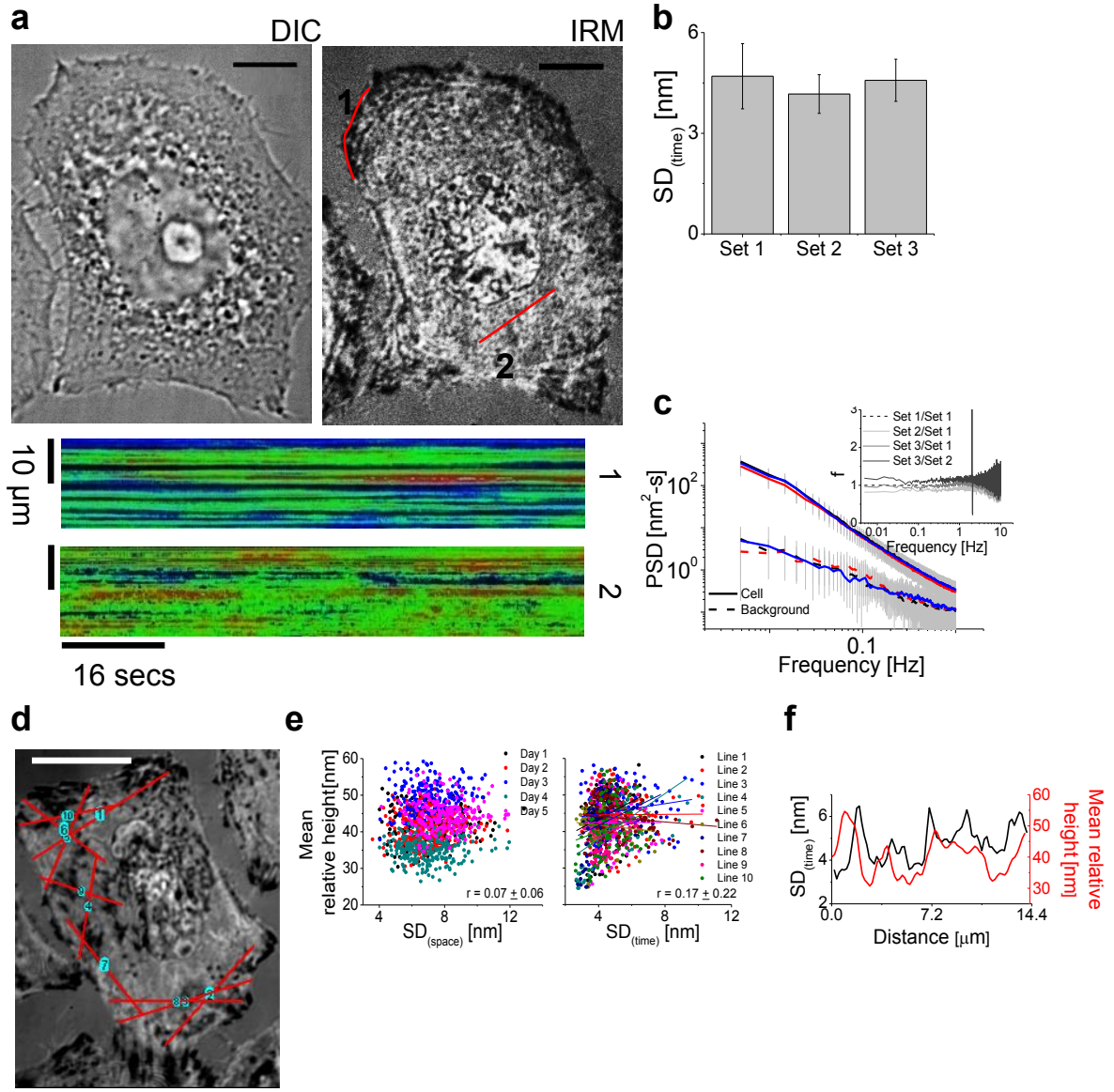

Figure S3. Temporal fluctuations and its variability.

(a) Representative images of a HeLa cell in the DIC and IRM modes (top). The temporal fluctuations across regions in a cell measured by kymographs at the marked ROIs, 1: on the focal adhesions and 2: inside the cell (bottom). (b) Temporal fluctuations across sets of experiments (N=10 cells each set) measured by $SD_{(time)}$. (c) Averaged PSDs of FBRs in cells across days and their backgrounds with inset showing *f* for the different days. (d) Line scans (red) in FBRs overlaid on a HeLa cell. Scale bar: 10 μm. (e) Plots of $SD_{(space)}$ vs. Mean relative height (left) and $SD_{(time)}$ vs. Mean relative height (right) with the average Pearson Correlation

Coefficient (r) mentioned in each. (f) The spatial profile of $SD_{(time)}$ (black) and Mean relative height (red) for two typical line scans.

Figure S4

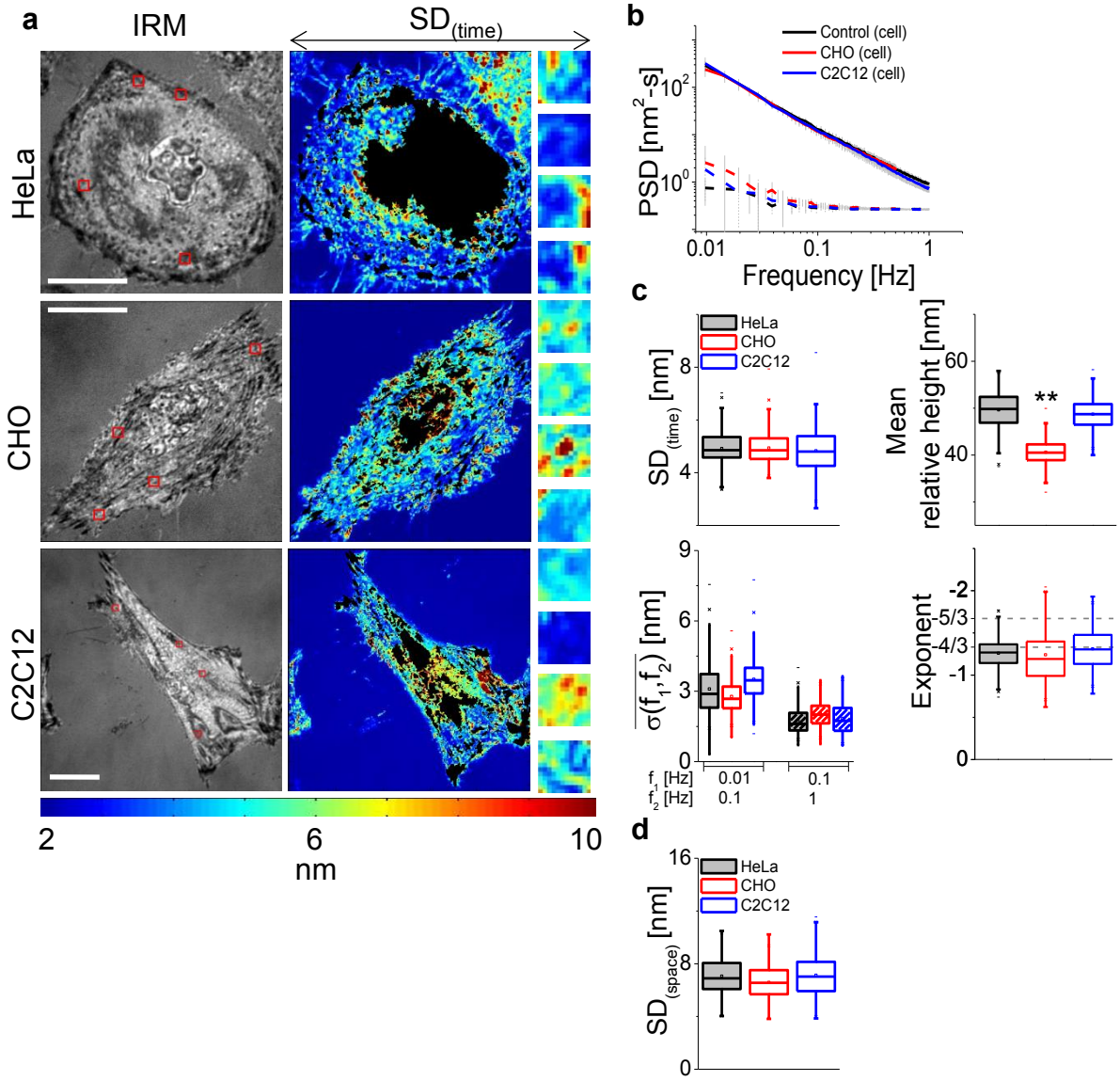

Figure S4. Similar trends of membrane fluctuations across three cell lines.

(a) IRM images (left, scale bar: 10 µm), $SD_{(time)}$ maps of the whole cells (middle, non-FBR regions blocked in black) and of four marked FBRs (right, scale bar: 1 µm) of HeLa, CHO and C2C12 cells. (b) The averaged PSDs of cells (N = 10 each, n_{HeLa} = 197 FBRs, n_{CHO} = 175 FBRs and n_{C2C12} = 219 FBRs, solid lines) and their respective backgrounds (dashed lines). (c) The

parameters of temporal fluctuations. (d) The parameters of spatial undulations. (** $p < 0.001$, One-way ANOVA). See also Table S4.

Table S2

Conditions	$\overline{\sigma(0.01Hz, 0.1Hz)}$	$\overline{\sigma(0.1Hz, 1Hz)}$	Exponent	$SD_{(time)}$	$SD_{(SD_{(time)})}$	Dissimilar pairs	$SD_{(space)}$	λ
	nm	nm		nm	nm	%	nm	nm
Control	3.0 ± 0.8	1.8 ± 0.5	-1.4 ± 0.3	5.0 ± 1.2	0.9 ± 0.3	63 ± 12	7.3 ± 1.7	505.5 ± 284.9
ATP dep.	2.1 ± 1.0	1.2 ± 0.4	-0.9 ± 0.2	3.9 ± 1.0	0.6 ± 0.4	59 ± 17	7.7 ± 2.3	478.0 ± 279.4
Cyto D	3.2 ± 0.8	2.4 ± 0.5	-1.3 ± 0.2	5.5 ± 0.8	1.1 ± 0.3	66 ± 14	7.9 ± 1.3	443.1 ± 173.7
Lat B	3.4 ± 0.8	2.5 ± 0.5	-1.3 ± 0.2	5.9 ± 0.8	1.1 ± 0.3	62 ± 13	7.9 ± 1.5	433.9 ± 183.0
Jas	2.9 ± 0.7	2.0 ± 0.4	-1.1 ± 0.2	4.3 ± 0.6	0.8 ± 0.3	65 ± 11	8.9 ± 1.5	450.6 ± 230.5
Blebb. (5 µM)	3.0 ± 0.7	1.7 ± 0.4	-1.3 ± 0.2	5.1 ± 0.7	0.9± 0.3	62 ± 8	7.9 ± 1.4	-
Blebb. (100 µM)	3.1 ± 0.9	1.7 ± 0.5	-1.3 ± 0.2	5.1 ± 0.9	1.1 ± 0.3	64 ± 10	7.9 ± 1.4	497.9 ± 240.4
Mitosis	2.3 ± 1.1	2.0 ± 0.5	-0.9 ± 0.9	4.8 ± 0.8	0.8 ± 0.3	67 ± 15	5.6 ± 2.2	418.2 ± 135.3

Parameters of temporal fluctuations and spatial undulations of HeLa cells under different conditions.

Cells highlighted in light and deep blue denote a significant decrease from the control with p-value < 0.05 and p-value < 0.001 respectively. Cells highlighted in yellow and red denote a significant increase from the control with p-value < 0.05 and p-value < 0.001 respectively. Parameters having values with no significant difference to the control are not highlighted. Mann-Whitney U test is done only on values of λ. For all the other parameters, a one-way ANOVA is done.

Figure S5

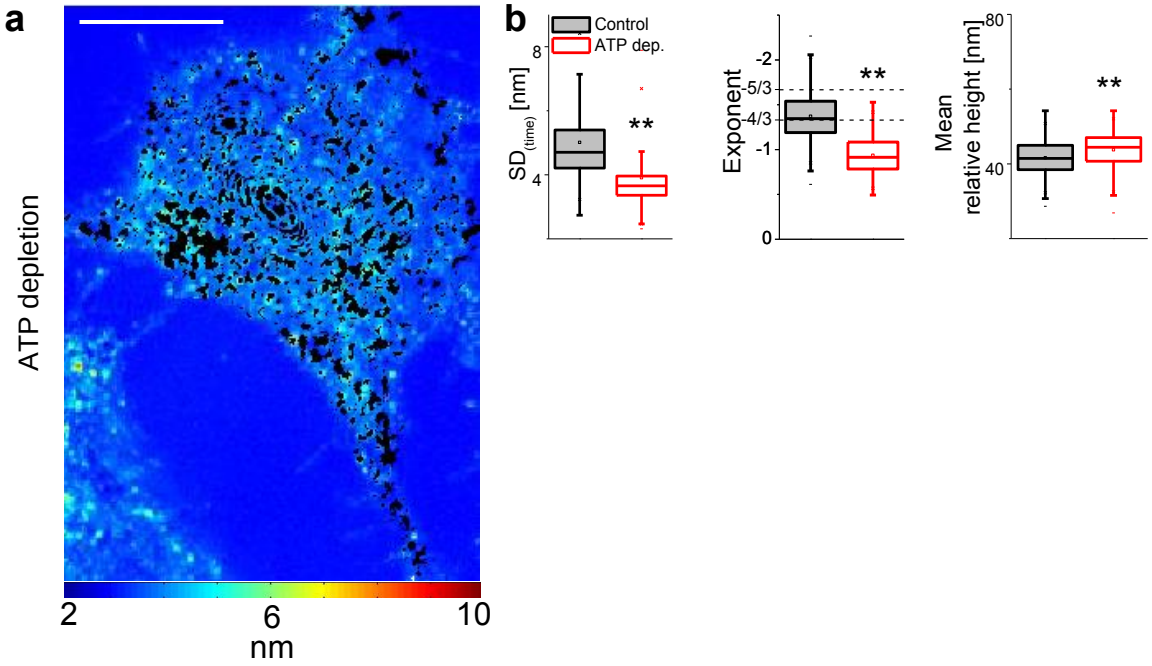

Figure S5. Detailed parameters of the effect of ATP driven processes on membrane fluctuations.

(a) Representative whole cell $SD_{(time)}$ map (non-FBR regions blocked in black) of an ATP depleted HeLa cell. Scale bar: 20 µm. (b) The parameters of temporal fluctuations ($SD_{(time)}$, Exponent and Mean relative height) in the two conditions (N = 30 cells each, $n_{control}$ = 854 FBRs, n_{ATPdep}= 964 FBRs). Asterisks indicate a significant difference (** $p<0.001$, one-way ANOVA). See also Tables S2 and S4.

Figure S6

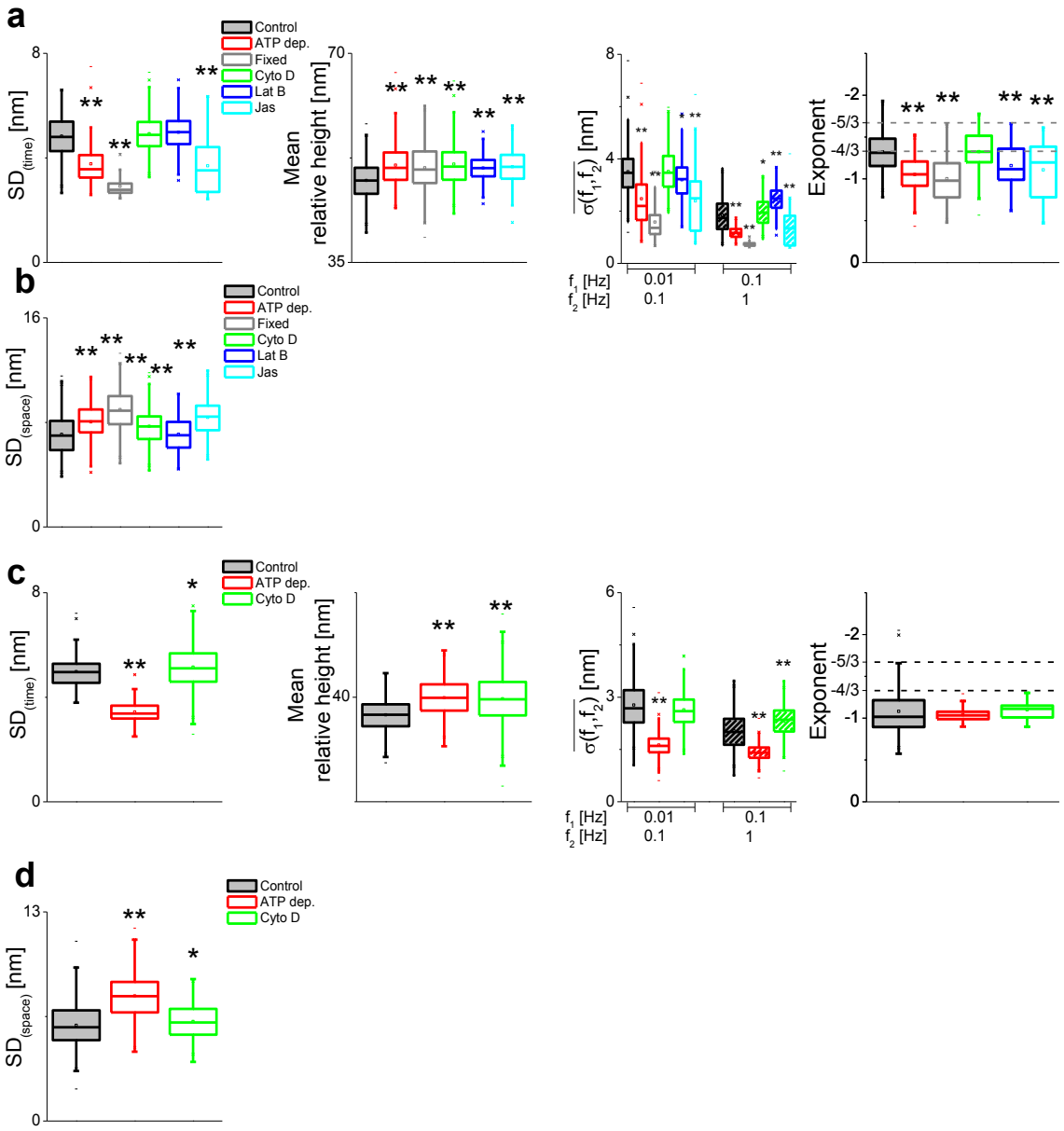

Figure S6. Detailed parameters of the behavior of cell lines under different conditions.

(a) The parameters of temporal fluctuations and (b) parameters of spatial undulations in C2C12 cells. (N = 10 cells each, $n_{control}$ = 219 FBRs, $n_{ATPdep.}$ = 139 FBRs, n_{fixed} = 171 FBRs, n_{CytoD} = 176 FBRs, n_{LatB} = 79 FBRs and n_{Jas} = 120 FBRs). (c) The parameters of temporal fluctuations and (d) parameters of spatial undulations in CHO cells. (N = 10 cells each, $n_{control}$ = 143 FBRs, $n_{ATPdep.}$ = 161 FBRs and n_{CytoD} = 137 FBRs). See also Table S4.

Figure S7

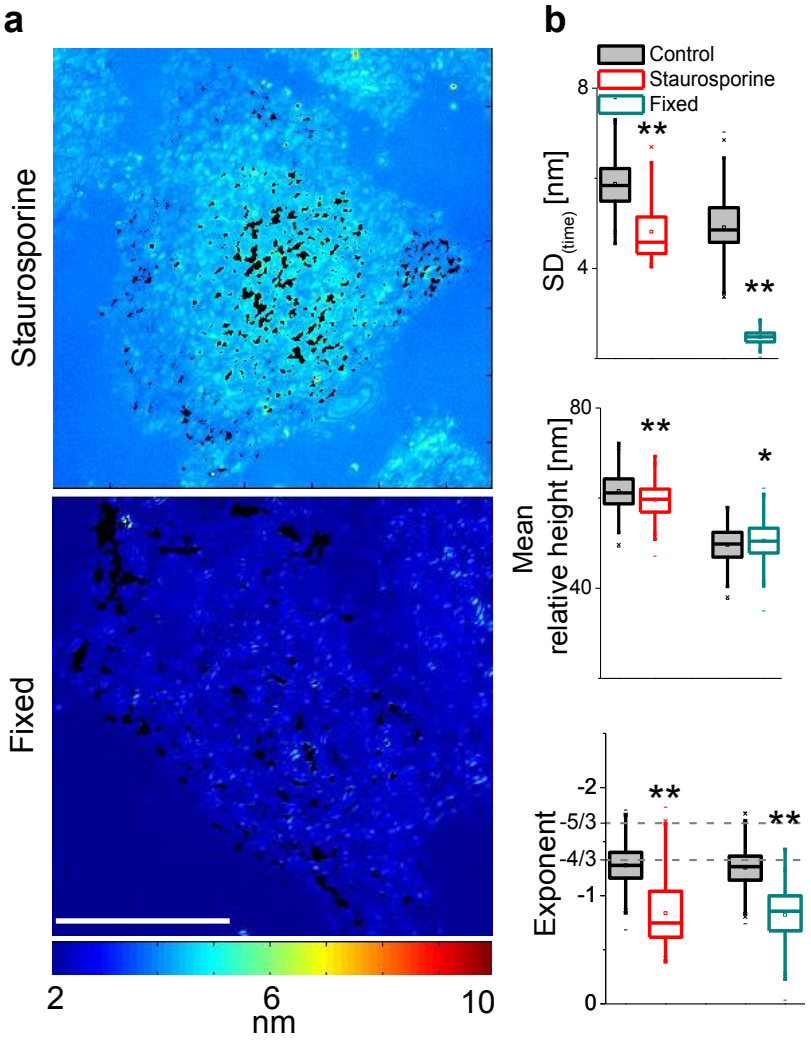

Figure S7. Detailed parameters capturing the effect of stopping cellular activity.

(a) Representative $SD_{(time)}$ maps (non-FBR regions blocked in black) of whole cells after Staurosporine treatment (left panel) and fixation (right panel). Scale bar: 10 µm. (b) The parameters of temporal fluctuations ($SD_{(time)}$, Mean relative height and Exponent) in the three conditions (N = 10 cells each, $n_{control}$ = 411 FBRs, $n_{staurosporine}$ = 310 FBRs and n_{fixed} = 331 FBRs). Asterisks indicate a significant difference (* $p < 0.05$, ** $p < 0.001$, One-way ANOVA). See also Tables S2 and S4.

Figure S8

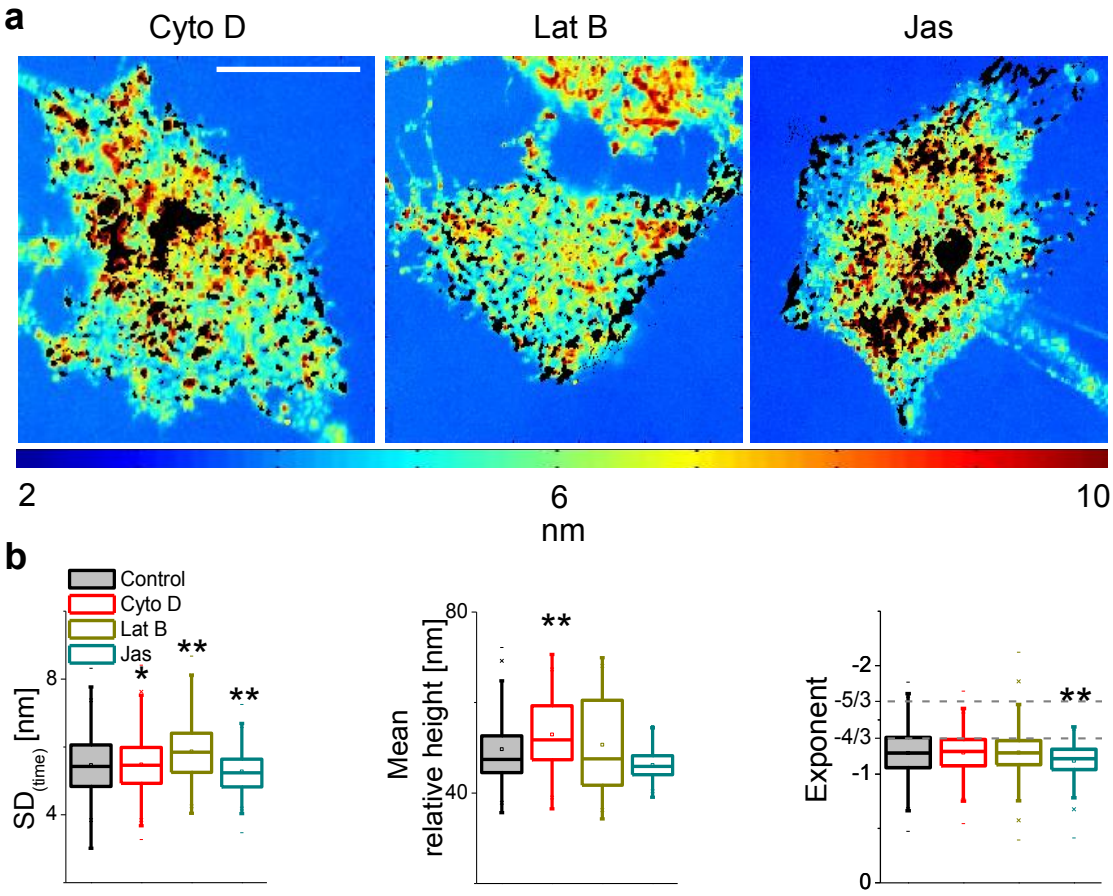

Figure S8. Detailed parameters on the effect of the cortex on membrane fluctuations.

(a) Representative $SD_{(time)}$ maps (non-FBR regions blocked in black) of a whole cell for Cyto D (left), Lat B (middle) and Jas (right) treated cells. Scale bar: 10 µm. (b) The parameters of temporal fluctuations ($SD_{(time)}$, Mean relative height and Exponent) in the different conditions (N = 30 each, $n_{control}$ = 770 FBRs, $n_{Cyto\ D}$ = 509 FBRs, $n_{Lat\ B}$ = 484 FBRs and n_{Jas} = 255 FBRs). Asterisks indicate a significant difference (* $p < 0.05$, ** $p < 0.001$, One-way ANOVA). See also Tables S2 and S4.

Figure S9

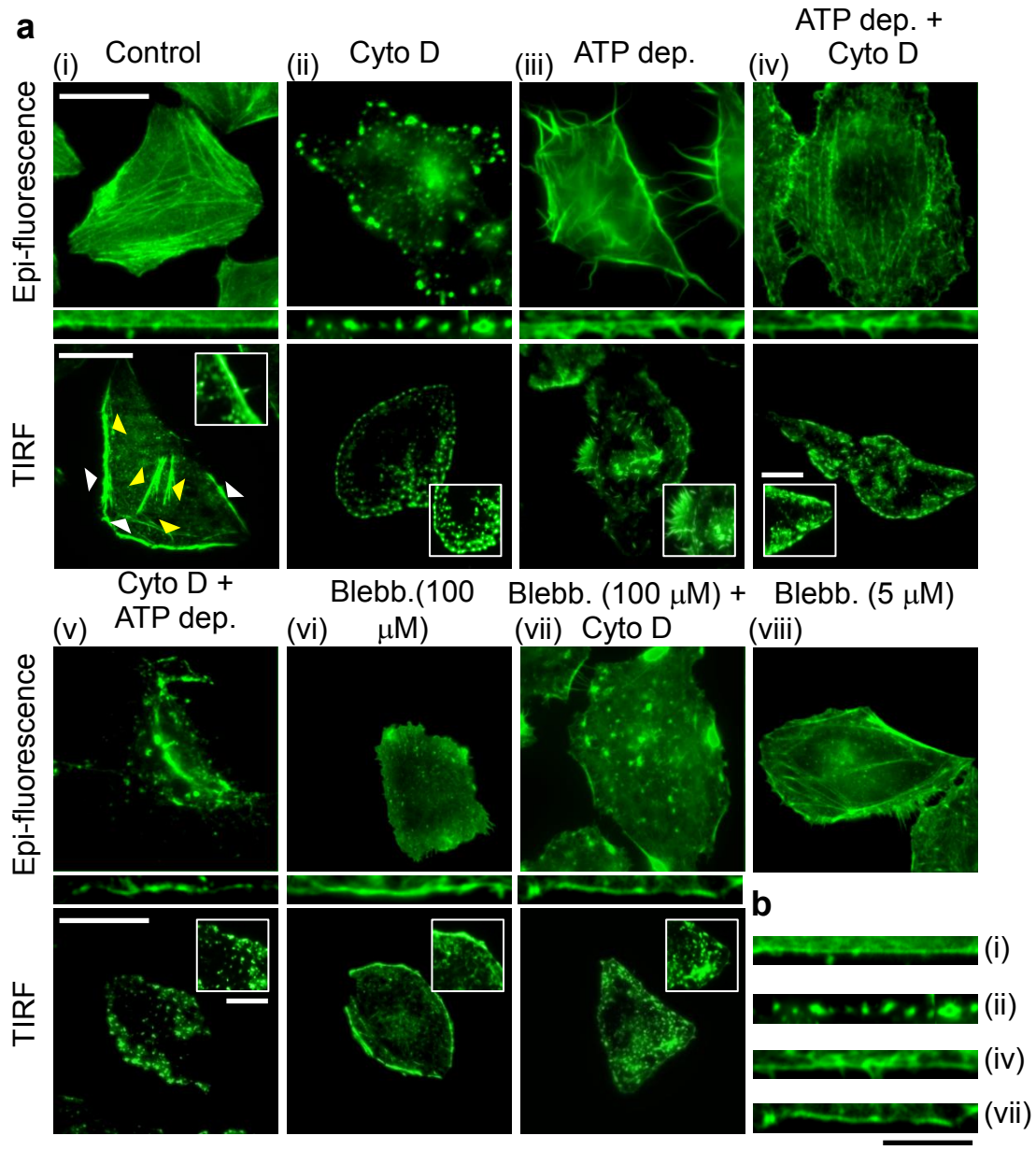

Figure S9. Quantification of cortical actin present under different conditions.

(a) Representative images of Alexa Fluor 488 Phalloidin stained cells captured in the Epi-fluorescence and TIRF (penetration depth 100 nm) modes in all the conditions (zoomed-in view in the inset, scale bar: 1 μm) along with linearized images of the cortical actin (middle) from the epi-fluorescent images. Scale bar: 10 μm. White arrowheads mark out the cortex at the edge while the yellow ones represent the stress fibres. (b) Representative images of the straightened cortex which show that pre-treatments stop cortex clearance on addition of Cyto D. Scale bar: 10 μm.

Figure S10

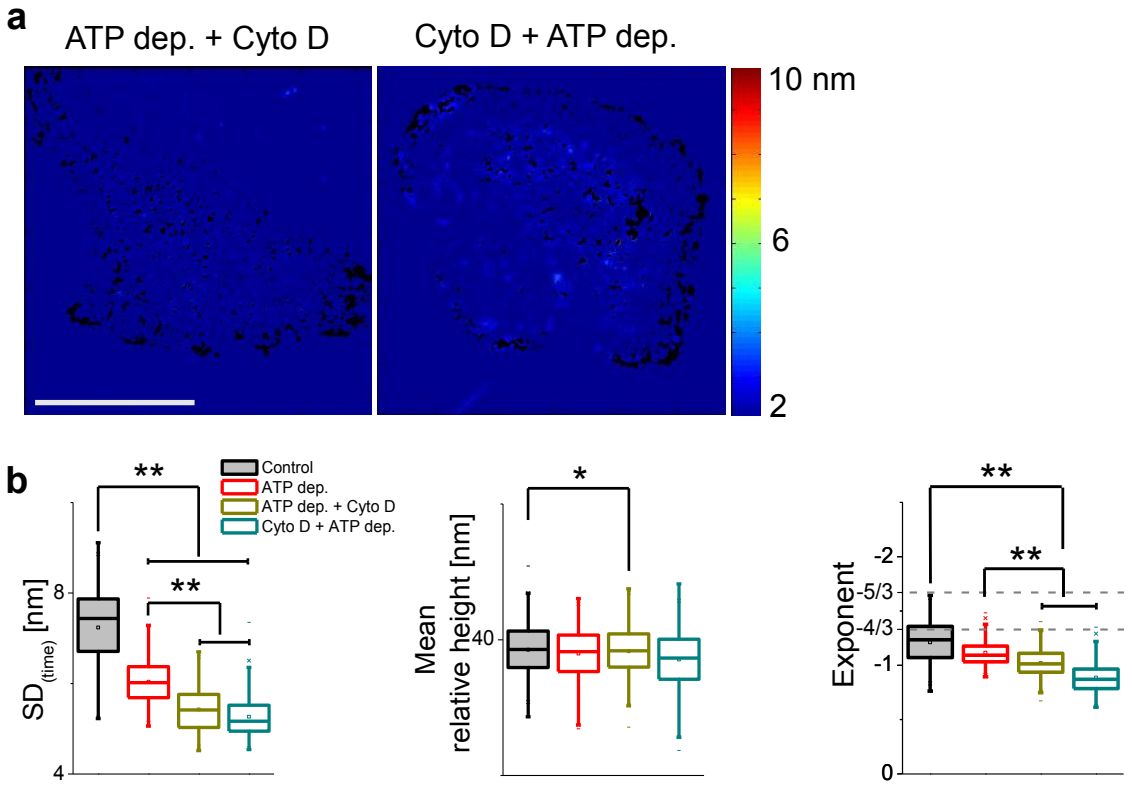

Figure S10. Detailed parameters towards the effect of polymerization while the Cyto D induced cortex clearance is blocked by ATP depletion.

(a) Representative $SD_{(time)}$ maps (non-FBR regions blocked in black) of a whole cell for ATP dep. + Cyto D treated (left) and Cyto D treated + ATP dep. (right) cells. Scale bar: 10 µm. (b) The parameters of temporal fluctuations ($SD_{(time)}$, Mean relative height and Exponent) in the different conditions (N = 10 each, $n_{control}$ = 119 FBRs, $n_{ATPdep.}$ = 158 FBRs, $n_{ATPdep.+Cyto\ D}$ = 254 FBRs and $n_{Cyto\ D+ATPdep.}$ = 162 FBRs). Asterisks indicate a significant difference (* $p < 0.05$, ** $p < 0.001$, One-way ANOVA). See also **Tables S2 and S4**.

Figure S11

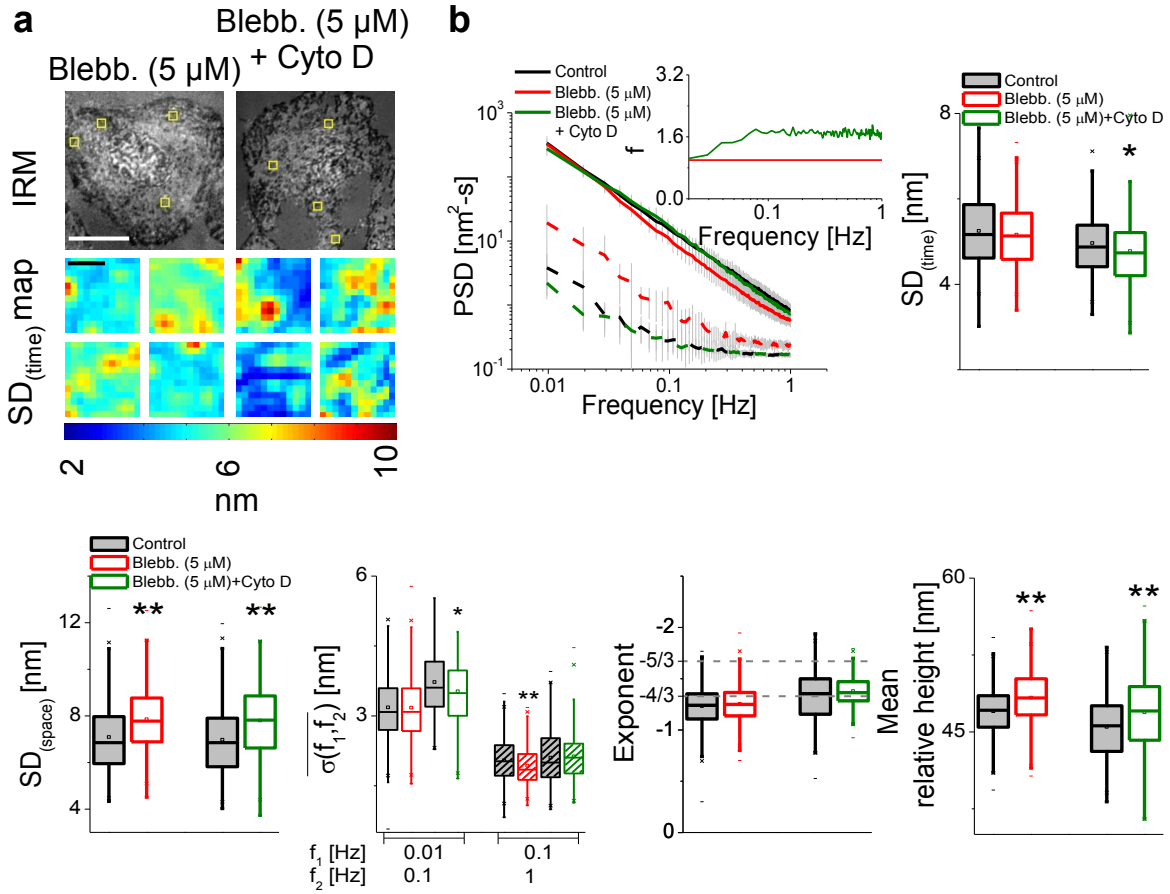

Figure S11. Low concentration of Blebb. affects fluctuations and does not stop cortex clearance by Cyto D.

(a) Representative IRM images (top, scale bar: 10 µm) and $SD_{(time)}$ maps (non-FBR regions blocked in black) of FBRs (bottom, scale bar: 1 µm) of control, Blebb. (5 µM), Cyto D after Blebb (5 µM) treated HeLa cells. (b) The averaged PSDs of cells (N = 10 each, $n_{control}$ = 175 FBRs, $n_{Blebb.}$ = 190 FBRs and $n_{Blebb.+CytoD}$ = 90 FBRs, solid lines) and their respective backgrounds (dashed lines); *f* in inset (Blebb. (5 µM) used as control for this measurement) with the parameters of spatio-temporal fluctuations. Asterisks indicate a significant difference (* $p < 0.05$, ** $p < 0.001$, One-way ANOVA). See also **Tables S2 and S4**.

Figure S12

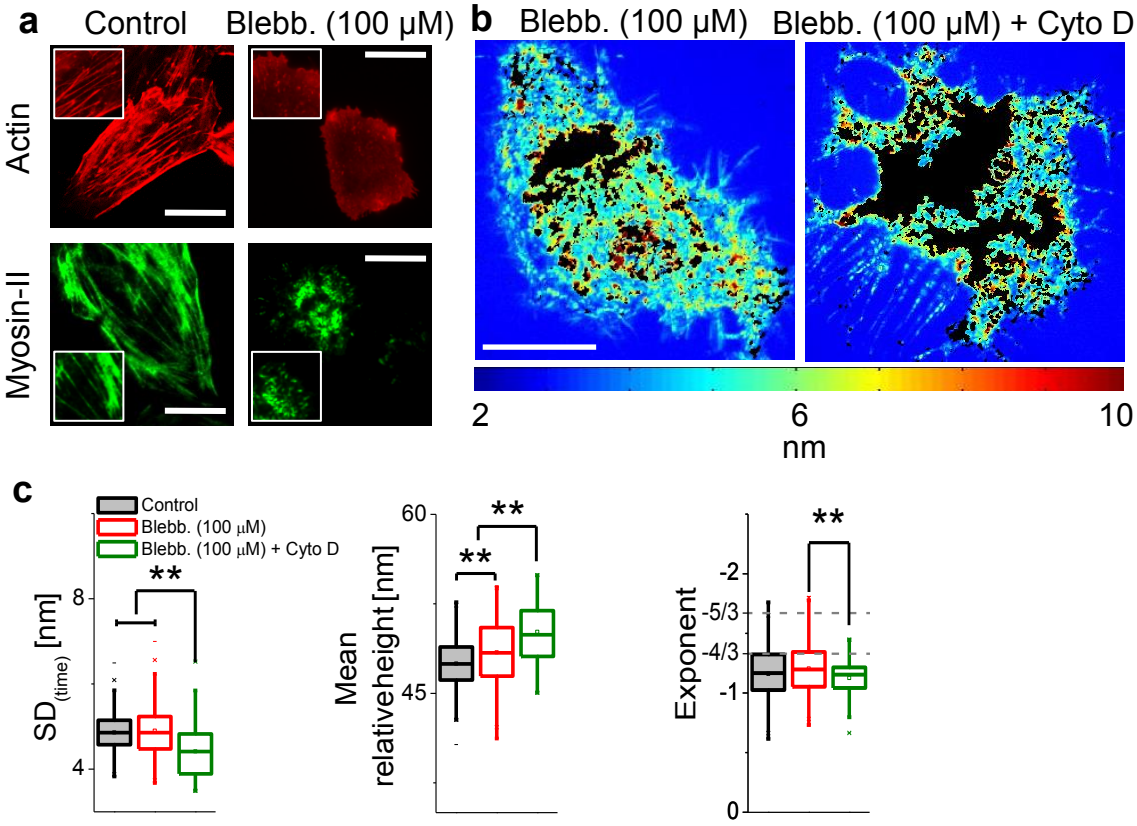

Figure S12. Detailed parameters towards the effect of polymerization on blocking Cyto D induced cortex clearance by pretreatment with Blebb. at a higher concentration.

(a) Representative epi-fluorescence images of actin (cells stained by Phalloidin-Rhodamine) and representative TIRF images of myosin II (cells transfected with pEGFP-mRLC1) in control and Blebb. (100 µM) treated HeLa cells. Scale bar: 10 µm. (b) Representative $SD_{(time)}$ maps (non-FBR regions blocked in black) of whole cells for Blebb. (100 µM) (left) and Blebb. (100 µM) + Cyto D treated (right) cells. Scale bar: 10 µm. (c) The parameters of temporal fluctuations ($SD_{(time)}$, Mean relative height and Exponent) in the different conditions (N = 10 each, $n_{control}$ = 165 FBRs, n_{Blebb} = 195 FBRs and $n_{Blebb+CD}$ = 72 FBRs). Asterisks indicate a significant difference (** $p < 0.001$, One-way ANOVA). See also **Tables S2 and S4**.

Figure S13

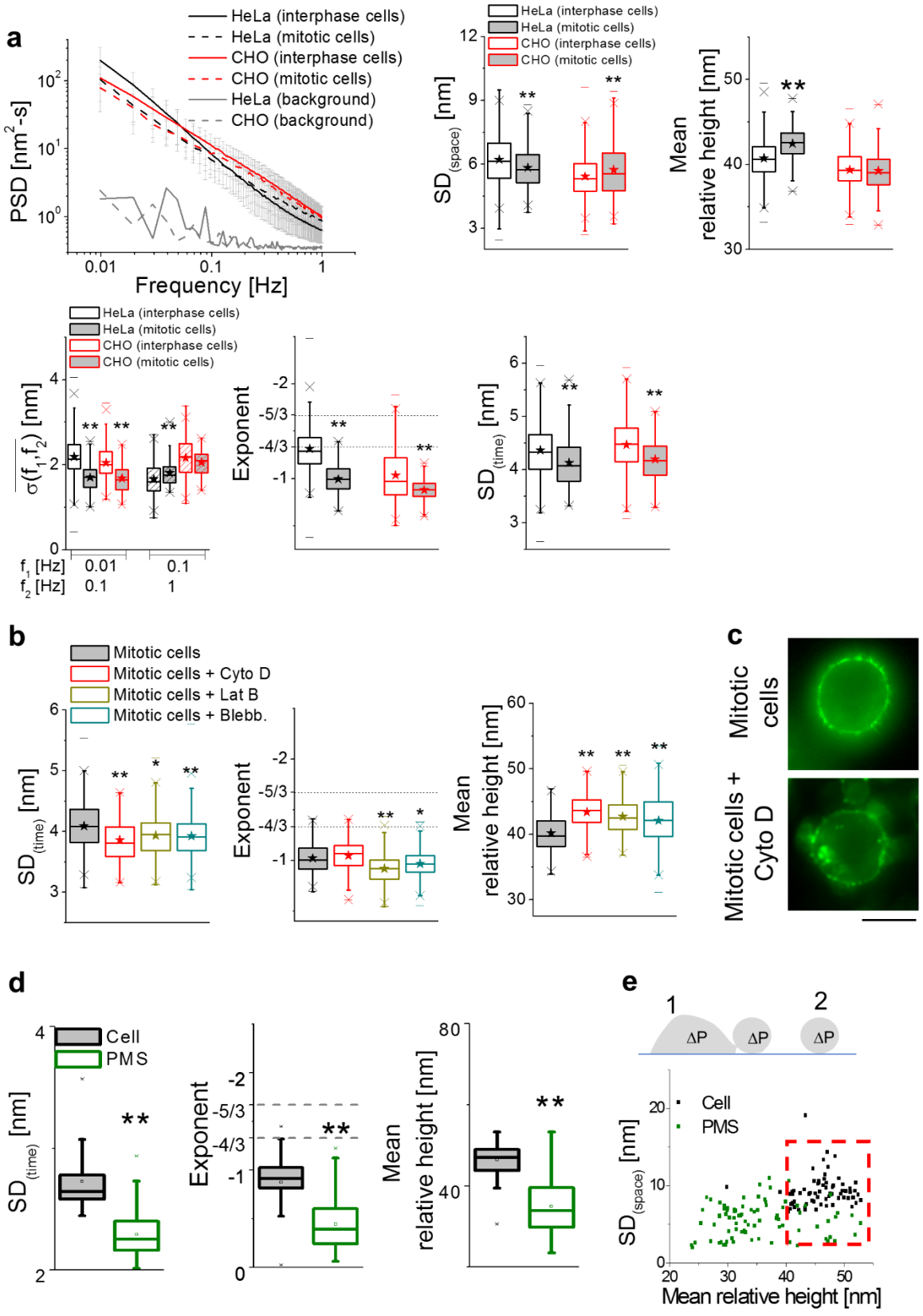
a
HeLa (interphase cells)
HeLa (mitotic cells)
CHO (interphase cells)
CHO (mitotic cells)
HeLa (background)
CHO (background)
PSD [nm²-s]
Frequency [Hz]
SD(space) [nm]
Mean relative height [nm]
σ(f1,f2) [nm]
Exponent
SD(time) [nm]
f1 [Hz] 0.01 0.1
f2 [Hz] 0.1 1
b
Mitotic cells
Mitotic cells + Cyto D
Mitotic cells + Lat B
Mitotic cells + Blebb.
c
Mitotic cells
Mitotic cells + Cyto D
d
Cell
PMS
e
ΔP
Cell
PMS
Mean relative height [nm]

Figure S13. Detailed parameters of membrane fluctuations during mitosis and in PMS.

(a) The averaged PSD of interphase (solid lines) and mitotic (dotted lines) HeLa (black) and CHO (red) cells with their backgrounds. Parameters of spatial undulations and temporal fluctuations of the interphase and mitotic cells in the two cell lines (N=10 cells each, $n_{interphase\ HeLa}$ = 328 FBRs, $n_{mitotic\ Hela}$ = 78 FBRs, $n_{interphase\ CHO}$ = 401 FBRs and $n_{mitotic\ CHO}$ = 60 FBRs). (b) The values of $SD_{(time)}$, Exponent and Mean relative height in mitotic cells, mitotic cells + Cyto D, mitotic cells + Lat B and mitotic cells + Blebb. (N = 15 cells each, $n_{mitotic\ cells}$ = 105 FBRs, $n_{,\ mitotic\ cells\ +\ Cyto\ D}$ = 85 FBRs, $n_{mitotic\ cells\ +\ Lat\ B}$ = 182 FBRs and $n_{mitotic\ cells\ +\ Blebb.}$ = 215 FBRs). (c) Representative images of mitotic cells stained with Alexa Flour 488 Phalloidin in the absence and presence of Cyto D. Scale bar: 10 µm. (d) The parameters of temporal fluctuations ($SD_{(time)}$, Exponent and Mean relative height) of cells and PMSs (N = 10 each, n_{cell} = 70 FBRs, n_{PMS} = 85 FBRs). ** mark a significant difference ($p<0.001$, One-way ANOVA). (e) Plot of $SD_{(space)}$ vs. mean relative height of cell derived PMS. Dotted region indicates cells and PMSs having the same relative height. Inset shows a schematic representation of a PMS pinched off but still adhered to the cell (1) and a cell free PMS (2) all having the same mean relative height and the same ΔP. See also **Tables S2 and S4**.

Figure S14

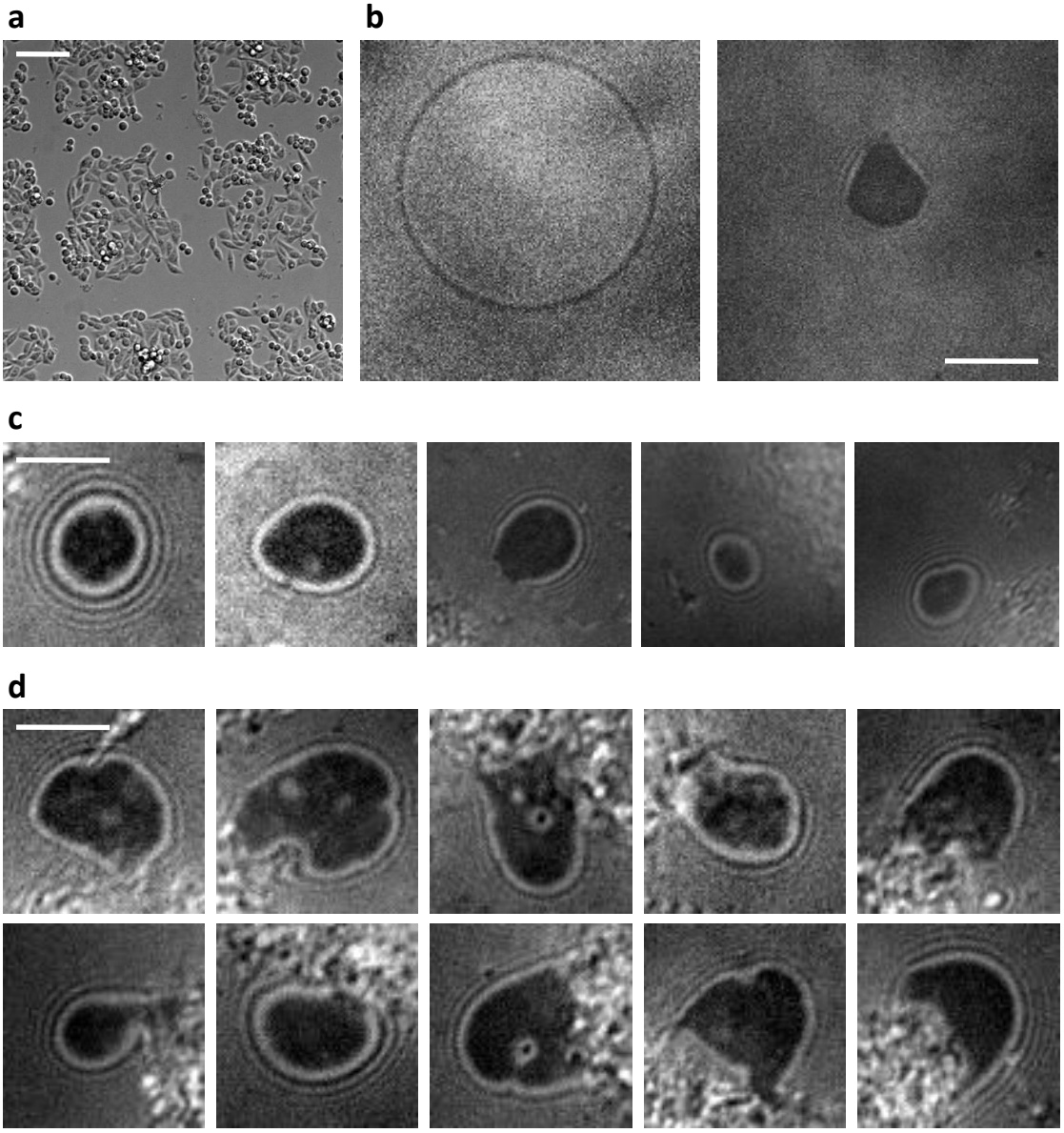

Figure S14. Types of PMSs.

(a) Micropatterned islands of CHO cells used for generating PMS. Scale bar: 30 μm. (b) Representative images of a PMS in DIC (left) and IRM (right) modes. Scale bar: 5 μm. (c) Representative IRM images of cell-free PMSs. Scale bar: 5 μm. (d) Representative IRM images of cell-attached PMSs. Scale bar: 5 μm.

Figure S15

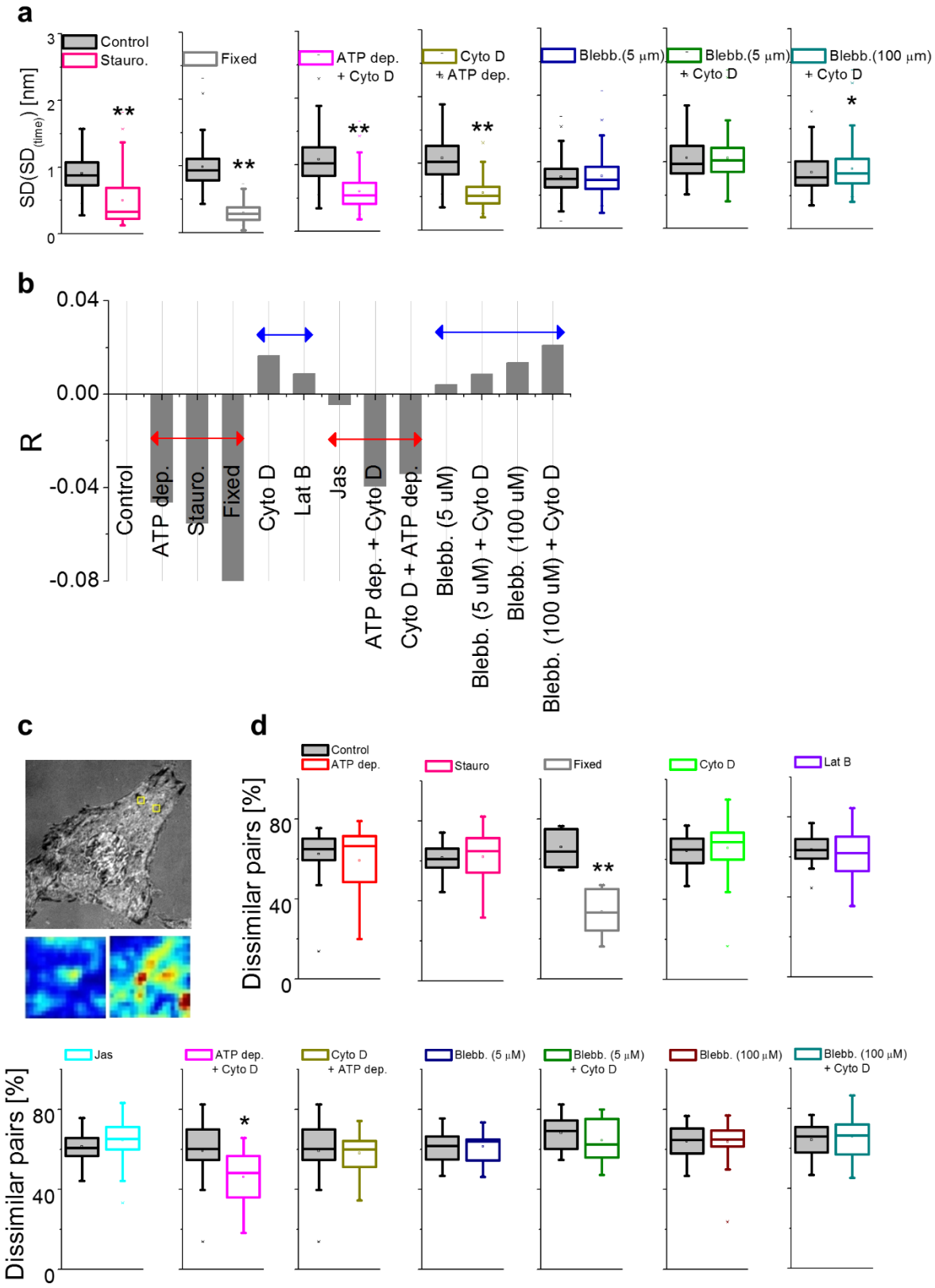
a
Control
Stauro.
Fixed
ATP dep.
+ Cyto D
Cyto D
+ ATP dep.
Blebb.(5 μm)
Blebb.(5 μm)
+ Cyto D
Blebb.(100 μm)
+ Cyto D
SD(SD(time)) [nm]
b
R
Control
ATP dep.
Stauro.
Fixed
Cyto D
Lat B
Jas
ATP dep. + Cyto D
Cyto D + ATP dep.
Blebb. (5 uM)
Blebb. (5 uM) + Cyto D
Blebb. (100 uM)
Blebb. (100 uM) + Cyto D
c
d
Dissimilar pairs [%]
Control
ATP dep.
Stauro
Fixed
Cyto D
Lat B
Jas
ATP dep.
+ Cyto D
Cyto D
+ ATP dep.
Blebb. (5 μM)
Blebb. (5 μM)
+ Cyto D
Blebb. (100 μM)
Blebb. (100 μM)
+ Cyto D

Figure S15. A measure of short and long length scale heterogeneities in cells.

(a) SD($SD_{(time)}$) for different conditions (N = 30 cells each). (b) Difference of ratio of SD($SD_{(time)}$) to Mean($SD_{(time)}$) of treated cells from that of control cell. $R = \left[\frac{SD(SD_{(time)})}{Mean(SD_{(time)})}\right]_{treated} - \left[\frac{SD(SD_{(time)})}{Mean(SD_{(time)})}\right]_{control}$. (c) Representative IRM image of a cell along with $SD_{(time)}$ maps of the two marked FBRs with the p-value measured to be 0.0009 by hypothesis testing (one-way ANOVA) of the $SD_{(time)}$ of the two. (d) Plots of the number of dissimilar pairs of FBRs (in %) between control and the treated sets. The parameters is calculated as $Dissimilar\ pairs = \frac{FBR\ pairs\ with\ SD_{(time)} having\ p<0.001}{Total\ no.\ of\ FBR\ pairs}$. * $p < 0.05$, ** $p < 0.001$, one-way ANOVA. See also **Tables S2 and S4**.

References

1. Limozin, L., and K. Sengupta. 2009. Quantitative reflection interference contrast microscopy (RICM) in soft matter and cell adhesion. ChemPhysChem. 10: 2752–2768.

2. Monzel, C., D. Schmidt, C. Kleusch, D. Kirchenbüchler, U. Seifert, A.-S. Smith, K. Sengupta, and R. Merkel. 2015. Measuring fast stochastic displacements of bio-membranes with dynamic optical displacement spectroscopy. Nat. Commun. 6: 8162.

3. Rodríguez-García, R., I.N. Ló Pez-Montero, M. Mell, G. Egea, N.S. Gov, and F. Monroy. 2015. Direct Cytoskeleton Forces Cause Membrane Softening in Red Blood Cells. Biophys. J. 108: 2794–2806.

4. Gov, N., A.G. Zilman, and S. Safran. 2003. Cytoskeleton confinement and tension of red blood cell membranes. Phys. Rev. Lett. 90: 228101.

5. Bicknese, S., N. Periasamy, S.B. Shohet, and A.S. Verkman. 1993. Cytoplasmic Viscosity Near the Cell Plasma Membrane: Measurement by Evanescent Field Frequency-Domain Microfluorimetry. Biophys. J. . 65: 1272–1282.

6. Kim, T., M.L. Gardel, and E. Munro. 2014. Determinants of Fluidlike Behavior and Effective Viscosity in Cross-Linked Actin Networks. Biophys. J. 106: 526–534.

7. Gov, N., and S.A. Safran. 2005. Red blood cell shape and fluctuations: Cytoskeleton confinement and ATP activity. J. Biol. Phys. 31: 453–464.

8. Betz, T., M. Lenz, J.-F. Joanny, and C.C. Sykes. 2009. ATP-dependent mechanics of red blood cells. PNAS. 106: 15320–15325.

9. Peukes, J., and T. Betz. 2014. Direct Measurement of the Cortical Tension during the Growth of Membrane Blebs. Biophys. J. 107: 1810–1820.

10. Lieber, A.D., S. Yehudai-Resheff, E.L. Barnhart, J.A. Theriot, and K. Keren. 2013. Membrane Tension in Rapidly Moving Cells Is Determined by Cytoskeletal Forces. Curr. Biol. 23: 1409–1417.

11. Fischer-Friedrich, E., A.A. Hyman, F. Jülicher, D.J. Müller, and J. Helenius. 2014. Quantification of surface tension and internal pressure generated by single mitotic cells. Sci. Rep. 6: 6213.